

How arbitrary are perturbative calculations of the electroweak phase transition?

Peter Athron^{a,b}, Csaba Balázs^b, Andrew Fowlie^a, Lachlan Morris^b,
Graham White^c, Yang Zhang^{d,e}

^a*Department of Physics and Institute of Theoretical Physics, Nanjing Normal University, Nanjing, Jiangsu 210023, China*

^b*School of Physics and Astronomy, Monash University, Melbourne 3800 Victoria, Australia*

^c*Kavli IPMU (WPI), UTIAS, The University of Tokyo, Kashiwa, Chiba 277-8583, Japan*

^d*School of Physics, Zhengzhou University, Zhengzhou 450000, China*

^e*CAS Key Laboratory of Theoretical Physics, Institute of Theoretical Physics, Chinese Academy of Sciences, Beijing 100190, China*

Abstract

We investigate the extent to which perturbative calculations of the electroweak phase transition are arbitrary and uncertain, owing to their gauge, renormalisation scale and scheme dependence, as well as treatments of the Goldstone catastrophe and daisy diagrams. Using the complete parameter space of the Standard Model extended by a real scalar singlet with a \mathbb{Z}_2 symmetry as a test, we explore the properties of the electroweak phase transition in general R_ξ and covariant gauges, OS and $\overline{\text{MS}}$ renormalisation schemes, and for common treatments of the Goldstone catastrophe and daisy diagrams. Reassuringly, we find that different renormalisation schemes and different treatments of the Goldstone catastrophe and daisy diagrams typically lead to only modest changes in predictions for the critical temperature and strength of the phase transition. On the other hand, the gauge and renormalisation scale dependence may be significant, and often impact the existence of the phase transition altogether.

Contents

| | | |
|----------|--|-----------|
| 1 | Introduction | 2 |
| 2 | The effective potential | 4 |
| 2.1 | $\overline{\text{MS}} + R_\xi$: The $\overline{\text{MS}}$ scheme in the standard R_ξ gauge | 7 |
| 2.2 | $\overline{\text{MS}} + \text{cov}$: The $\overline{\text{MS}}$ scheme in the covariant gauge | 8 |
| 2.3 | HT: The high-temperature approximation | 9 |
| 2.4 | PRM: The \hbar expansion | 10 |
| 2.5 | OS-like: The on-shell-like scheme | 11 |
| 3 | Modifications to the effective potential | 12 |
| 3.1 | Goldstone catastrophe | 12 |
| 3.2 | Daisy diagrams | 13 |
| 3.3 | Renormalisation group equations | 14 |
| 4 | Results | 14 |
| 4.1 | Gauge dependence | 14 |
| 4.2 | Renormalisation scale dependence | 19 |
| 4.3 | Daisy resummation dependence | 25 |
| 4.4 | Comparison of renormalisation schemes and other methods | 25 |
| 4.5 | Comparison in whole parameter space | 27 |
| 5 | Conclusions | 30 |
| A | Phase structure | 32 |
| B | Benchmark point | 33 |
| C | Mass spectrum | 34 |
| D | Numerical uncertainties | 36 |
| | References | 37 |

1 Introduction

A central motivation for the ambitious program of the next generation experiments that probe physics beyond the Standard Model (SM) is to understand aspects of electroweak symmetry breaking in the cosmological context [1–3]. If the electroweak phase transition (EWPT) was strongly first order, it would satisfy Sakharov’s third condition for baryogenesis [4] and the collision of sound shells could create a stochastic gravitational wave background that is expected to peak at a frequency range visible to LISA [1]. In the SM, however, the EWPT is predicted to be a crossover [5–9] and new states near the electroweak scale would be needed to change it to a strong first-order transition [10–47]. Either a 27 TeV upgrade to the LHC [48] or the ambitious 100 TeV proposal [49] could potentially confirm the SM prediction [5–9].

Phenomenological studies usually assess the impact of new states on the EWPT through the perturbative effective potential. As has long been recognised, the perturbative effective potential depends on a choice of gauge and gauge fixing parameter ξ [50], a choice of renormalisation scheme [51, 52] and a choice of renormalisation scale [53]. Besides these choices, there are different ways to remedy infrared (IR) divergences caused by Goldstone boson loops and different treatments of daisy diagrams [54]. These subjective factors lead to theoretical uncertainties and a degree of arbitrariness associated with the perturbative EWPT predictions. For a recent update on non-perturbative approaches, see Ref. [55, 56]. An effective field theory approach is also being developed that promises a gauge-independent evaluation of the effective potential free of some of the problems of the traditional approaches [55–59].

In this work we are predominantly motivated by the possibility of a first-order EWPT. In that case, the ground state makes a discontinuous jump while electroweak symmetry breaks. As is customary, we characterise a transition by a critical temperature, below which the transition is possible, and a transition strength. More detailed descriptions could include, for example, the latent heat, which characterises the energy available to phenomena such as gravitational waves, and the nucleation temperature. A critical temperature is defined as any temperature at which the effective potential contains two degenerate minima, i.e.,

$$V(\Phi, T_c) = V(\Theta, T_c), \quad (1)$$

where Φ and Θ are distinct locations in the field space where the potential has a minimum at the temperature T_c . For non-manifestly gauge covariant calculations the strength of the transition is typically quantified by

$$\gamma_{\text{EW}} = \frac{\sqrt{\sum_i (\Phi_i - \Theta_i)^2}}{T_c}, \quad (2)$$

where the sum only includes components of the fields that break EW symmetry. We compute T_c and γ_{EW} numerically from the effective potential using **PhaseTracer**; see the manual [60] for an overview of the numerical methods used. For the purposes of the work described here we extended¹ **PhaseTracer** to include other approaches such as the so called \hbar expansion approach of Ref. [50]. These features should be available in a future release of **PhaseTracer** and are not to our knowledge implemented in any other public software.

In this work, for the first time we present a comprehensive study of uncertainties that arise in the simplest widely used techniques in theoretical calculations.² Such techniques include gauge-independent methods that lack resummation at leading order [50] and gauge-dependent methods that include leading-order resummation. Additionally, we examine numerical differences arising from different renormalisation schemes and gauge sensitivity arising from R_ξ and covariant gauges and gauge-dependent tadpole constraints. Quantifying gauge dependence is difficult, as although there are indications from perturbativity, it is unclear how much to change the gauge parameter. Our investigation

¹The code for this is in the development branch of our github repository and will later be released in a future stable version.

²For example, we do not consider lattice calculations, or the \hbar -expansion in dimensional reduction.

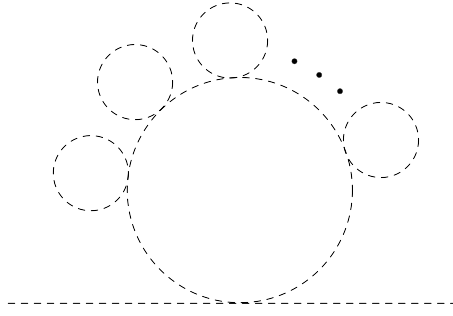


Figure 1: Daisy contributions to the two-point function from the quartic interaction. Each additional loop contributes a factor $\lambda T^2/m^2$, spoiling perturbativity unless appropriately resummed.

of renormalisation scheme and scale dependence, and the two gauge-independent approaches, on the other hand, do not depend on these choices. Approximate as they may be, such techniques are fast and simple and have been used in phenomenological analyses in many models, including large multi-parameter scans. It is therefore useful to understand the pros and cons in each case, and based on this information we leave it to the reader to decide the most appropriate method for their analysis.

As our benchmark model, we consider the SM augmented by a real scalar singlet (the SSM) and a \mathbb{Z}_2 discrete symmetry imposed on the potential. This model is ideal in its simplicity for highlighting key features of the parameter space as it includes both tree-level and thermal barriers depending on whether the discrete symmetry is broken at non-zero temperatures (but is enforced at zero temperature). It also includes cases where the gauge boson thermal loops are sufficiently important that gauge dependence might become crucial, as it does in the SM with a light Higgs boson [50]. We build on recent progress in examining the impact of theoretical uncertainties on the EWPT. The gauge dependence of tunneling rates and the implications for gravitational wave signals in gauge-dependent techniques were examined in Ref. [61–63] and the scale dependence in multiple models was investigated in Ref. [64–66]. Here, we consider the combined impacts of choices of scale, gauge and gauge fixing parameter, treatment of higher-order daisies, and the Goldstone catastrophe (GC).

The paper is organised as follows. In Sec. 2 we define our model and discuss various treatments of the effective potential, including choices of renormalisation scheme and gauge. In Sec. 3, we describe modifications to the effective potential to account for daisy diagrams and avoid the GC. In Sec. 4, we show our numerical results on the impact of the choice of renormalisation scheme, scale, resummation methods, and gauge. Finally, the conclusions and discussions are given in Sec. 5.

2 The effective potential

Evidently, analysing the dynamics of the phase transition requires an accurate treatment of the effective potential. In the following subsections, we discuss the methods considered in this paper. Unfortunately, all methods suffer from some of the following potential theoretical ambiguities:

1. Gauge dependence — the effective potential is fundamentally gauge dependent as it only contains one-particle irreducible loop diagrams. This omits external leg corrections that would otherwise maintain gauge independence. The choice of gauge can strongly impact the EWPT predictions; for example, in the SM the strength of the EWPT at leading order is proportional to terms involving the gauge parameter, $\xi^{3/2}$ [50].³
2. Scale dependence — the one-loop potential and resulting phenomenological predictions could strongly depend on the scale Q and choice of renormalisation scheme. The dependence originates from regularizing the loop corrections in a particular scheme, as usual.
3. Linde’s infamous IR problem [67] — the perturbative expansion may break down near the critical temperature. The loop expansion involves the mode occupation $g \rightarrow gn_B \sim gT/m$ for gauge bosons and $\lambda \rightarrow \lambda T^2/m^2$ for scalars as shown in the daisy diagram in Fig. 1.⁴ This expansion diverges when $T \gg m$. Specifically the Goldstone contributions can get large deep in the broken phase and the gauge boson contributions can get large for small field values when $m \simeq 0$. There exists two prescriptions that alleviate Linde’s IR problem by resumming the most dangerous daisy diagrams to all orders; see Sec. 3.2.
4. Goldstone catastrophe (GC) [69–71] — Goldstone bosons could be massless, e.g., in the $\xi = 0$ gauge in the tree-level vacuum, and lead to divergences in the second-derivatives of the potential. Although terms in one-loop corrections to the potential of the form $x^2 \ln x \rightarrow 0$ vanish as $x \rightarrow 0$, the second derivatives diverge, meaning that we could not compute e.g., the Higgs masses at one-loop. Whilst the photon is also massless, its mass isn’t field-dependent, and doesn’t lead to these problems. See Sec. 3.1 for a discussion of the treatments of this problem considered in this work.
5. Tadpole constraints — fixing parameters to ensure agreement at one-loop with experimentally measured Higgs mass and vacuum expectation value (VEV) can reintroduce gauge dependence if not done carefully, even in an otherwise gauge-independent method (see Sec. 2.4). To do so one should only impose the tadpole conditions at tree-level. However in this case one must include one-loop tadpoles diagrams in corrections to the masses and other loop calculations.

The occurrences of these problems in the treatments in this paper are summarised in Tab. 1. In addition, uncertainties on the SM nuisance parameters, such as the top mass, result in parametric uncertainties.

The benchmark model (the SSM) used in our calculations is the SM extended by a real scalar singlet. The tree-level Higgs potential for the Higgs doublet and the real scalar field respects a \mathbb{Z}_2 symmetry, $S \rightarrow -S$,

$$V_0(H, S) = -\mu_h^2 H^\dagger H + \lambda_h (H^\dagger H)^2 - \frac{\mu_s^2}{2} S^2 + \frac{\lambda_s}{4} S^4 + \frac{\lambda_{hs}}{2} H^\dagger H S^2. \quad (3)$$

³Though Ref. [61] notes that such terms come with opposite signs and that the gauge dependence isn’t strong for gauges consistent with a perturbative expansion.

⁴In the SM it is common to use $\lambda \sim g^2$ which reduces the theory to power counting in a single coupling. This though is model dependent, see for instance Ref. [68].

| Name | Order | ξ dependence | μ dependence | Concern |
|-------------------------------------|----------------------------------|------------------|------------------|--------------------------|
| PRM | Tree minima; 1-loop potential | Tadpoles | Explicit | No daisies |
| High- T | 1-loop leading terms | Tadpoles | Implicit | Accuracy |
| $\overline{\text{MS}}$ | 1-loop potential | Explicit | Explicit | ξ & μ dependence |
| $\overline{\text{MS}} + \text{RGE}$ | 1-loop potential; 2-loop RGE | Explicit | Reduced by RGE | ξ dependence |
| OS | 1-loop potential | Explicit | No | ξ dependence |
| Covariant gauge | 1-loop potential | Explicit | Explicit | ξ & μ dependence |

Table 1: Comparison of perturbative treatments of the effective potential explored in this work. In the final column, we show our initial concerns about the treatment that we investigate in detail in Sec. 4.

Note the convention of the negative sign in front of the μ_h^2 and μ_s^2 terms. Denoting the fields as

$$H = \frac{1}{\sqrt{2}} \begin{pmatrix} G^\pm \\ \phi_h + iG^0 \end{pmatrix} \quad \text{and} \quad S = \phi_s, \quad (4)$$

where we treat ϕ_h and ϕ_s as real background fields, the tree level effective potential takes the form

$$V_0(\phi) = -\frac{\mu_h^2}{2}\phi_h^2 + \frac{\lambda_h}{4}\phi_h^4 - \frac{\mu_s^2}{2}\phi_s^2 + \frac{\lambda_s}{4}\phi_s^4 + \frac{\lambda_{hs}}{4}\phi_h^2\phi_s^2, \quad (5)$$

where $\phi \equiv (\phi_h, \phi_s)$.

We impose constraints on the free parameters in the potential to fix the masses of the scalar particles and the vacuum. First, we require that at zero temperature an extremum occurs at $\phi_h = v_h \simeq 246 \text{ GeV}$ and $\phi_s = v_s = 0$,

$$\left. \frac{\partial V}{\partial \phi_h} \right|_{\mathbf{v}} = 0 \quad \text{and} \quad \left. \frac{\partial V}{\partial \phi_s} \right|_{\mathbf{v}} = 0, \quad (6)$$

where $\mathbf{v} \equiv (v_h, v_s)$ and the potential is to be evaluated at $T = 0$. We could impose this constraint on the tree-level or one-loop potential. The second condition in eq. (6) is satisfied trivially with a vanishing singlet VEV, while, at tree-level, the first condition for the Higgs requires,

$$\mu_h^2 = \lambda_h v_h^2. \quad (7)$$

We only fix the zero-temperature vacuum in our model — at finite temperature the vacuum needn't satisfy eq. (6). Typically, at high-temperature the vacuum lies at the origin, $\phi = (0, 0)$. As the Universe cools, there is a smooth transition in the singlet direction, $(0, 0) \rightarrow (0, v_s(T))$. From that state, there is the possibility of a FOPT that breaks EW symmetry, $(0, v_s(T)) \rightarrow (v_h(T), 0)$. Subsequently, the ground state smoothly evolves to the desired $(v_h, 0)$ state at zero temperature. This was demonstrated to be the only possible pathway for a FOPT in a high-temperature approximation [72]. For further discussion see appendix A.

Second, we require that the vacuum reproduces the experimentally measured Higgs mass, $m_h = 125.25 \text{ GeV}$ [73], and the desired scalar singlet mass, which we treat as an

input in this work. If we neglect the momentum in the self energy (see remarks in Sec. 3.3 detailing the impact of this approximation) this corresponds to,

$$\left. \frac{\partial^2 V}{\partial \phi_h^2} \right|_v = m_h^2 \quad \text{and} \quad \left. \frac{\partial^2 V}{\partial \phi_s^2} \right|_v = m_s^2. \quad (8)$$

To ensure the potential has the correct form for this we eliminate the λ_h quartic by fixing m_h and exchange μ_s^2 for the singlet mass m_s . This leaves only m_s , λ_s and λ_{hs} as free parameters in our model.

The desired squared masses are positive, which ensures the zero-temperature VEVs correspond to minima of the potential. After fixing the Lagrangian parameters, we check that the global minimum of the potential at zero temperature is

$$\langle \phi_h \rangle = v_h \simeq 246 \text{ GeV} \quad \text{and} \quad \langle \phi_s \rangle = v_s = 0, \quad (9)$$

as desired. We may impose eq. (8) on the tree-level or one-loop potential. The tree-level scalar masses are

$$\overline{m}_h^2 = -\mu_h^2 + 3\lambda_h v_h^2 = 2\lambda_h v_h^2, \quad (10)$$

$$\overline{m}_s^2 = -\mu_s^2 + \frac{\lambda_{hs}}{2} v_h^2. \quad (11)$$

where we use $\overline{m}_{h,s}$ to emphasise that these are scheme-dependent tree-level masses. When solving this at higher order with the one-loop Higgs pole mass and one-loop tadpoles, we numerically solve for λ_h including the one-loop tadpoles iteratively. We detail treatments of the one-loop corrections to this potential in the following subsections.

2.1 $\overline{\text{MS}} + R_\xi$: The $\overline{\text{MS}}$ scheme in the standard R_ξ gauge

This is a standard treatment of the effective potential. The one-loop corrections to the potential in the standard R_ξ [74] gauges⁵ and $\overline{\text{MS}}$ scheme are given by [50, 53]

$$\begin{aligned} V_{\text{CW}}(\phi) = \frac{1}{64\pi^2} & \left[\sum_{i \in h} n_i m_i^4(\phi, \xi) \left(\log \left(\frac{m_i^2(\phi, \xi)}{Q^2} \right) - \frac{3}{2} \right) \right. \\ & + \sum_{i \in V} n_i m_i^4(\phi) \left(\log \left(\frac{m_i^2(\phi)}{Q^2} \right) - \frac{5}{6} \right) \\ & - \sum_{i \in V_L} n_i (\xi m_i^2(\phi))^2 \left(\log \left(\frac{\xi m_i^2(\phi)}{Q^2} \right) - \frac{3}{2} \right) \\ & \left. - \sum_{i \in f} n_i m_i^4(\phi) \left(\log \left(\frac{m_i^2(\phi)}{Q^2} \right) - \frac{3}{2} \right) \right], \end{aligned} \quad (12)$$

⁵Although we refer to this as the standard R_ξ gauges, it is important to note that we do not use fixed VEVs in the gauge fixing Lagrangian, as is standard when calculating most observables. However since the field in the effective potential should be allowed to vary, the use of a fixed VEV would spoil cancellations of the mixing between the scalar (goldstones) and the gauge sectors, so instead the field is allowed to fluctuate away from the minimum. Although we still refer to this as the standard R_ξ gauge here, it is sometimes referred to as the background field R_ξ gauge in the literature, see e.g. [75], to distinguish it from the case with a fixed VEV.

where Q is the renormalisation scale and \overline{m}_i are field-dependent $\overline{\text{MS}}$ masses (for their specific forms in our model see appendix C), and we have suppressed the scale dependence of the masses. The sum over h represents a sum over the scalar fields, which at the electroweak breaking minimum can be separated into physical Higgs and Goldstone bosons. The sum over V includes transverse and longitudinal massive gauge bosons. The gauge dependent sum over V_L includes longitudinal gauge bosons. Lastly, the sum over f includes relevant fermion fields.

The one-loop thermal corrections in the R_ξ gauge are

$$V_T(\phi, T) = \frac{T^4}{2\pi^2} \left[\sum_{i \in h} n_i J_B \left(\frac{m_i^2(\phi, \xi)}{T^2} \right) + \sum_{i \in V} n_i J_B \left(\frac{m_i^2(\phi)}{T^2} \right) - \sum_{i \in V_L} n_i J_B \left(\frac{\xi m_i^2(\phi)}{T^2} \right) + \sum_{i \in f} n_i J_F \left(\frac{m_i^2(\phi)}{T^2} \right) \right]. \quad (13)$$

Note that in the tree-level minimum, the Goldstone boson masses are proportional to the corresponding gauge boson masses and ξ (i.e. $m_G^2(\phi, \xi) = \xi m_V^2(\phi)$), and that $n_G = n_{V_L}$, such that the ξ -dependence vanishes in eqs. (12) and (13), as expected from Nielsen's identity.

We construct the total effective potential by adding the one-loop terms to the tree-level potential,

$$V(\phi, T) = V_0(\phi) + V_{\text{CW}}(\phi) + V_T(\phi, T). \quad (14)$$

Additionally, there are further possible modifications to the potential to treat the GC and resum daisy diagrams; see Sec. 3.

2.2 $\overline{\text{MS}}$ + cov: The $\overline{\text{MS}}$ scheme in the covariant gauge

The previous $\overline{\text{MS}}$ treatment considered the standard R_ξ gauge. The standard R_ξ gauge used for effective potentials includes scalar fields that we vary in the gauge fixing Lagrangian. However this means that a different gauge is used for calculating the potential at each field value, which may be a cause for some concern [54, 76, 77].⁶ To remedy this, the effective potential of the SSM using the covariant gauge (sometimes called the Fermi gauges in the literature) [76–79] in the $\overline{\text{MS}}$ scheme has been used in recent work [48]. The gauge fixing Lagrangian in this gauge is,

$$\mathcal{L}_{\text{g.f.}} = -\frac{1}{2\xi_W}(\partial^\mu W_\mu^a)^2 - \frac{1}{2\xi_B}(\partial^\mu B_\mu)^2. \quad (15)$$

This avoids the issue of a fixed VEV at the expense of mixing between the Goldstones and the gauge sector. We here use the same potential as derived in Ref. [48], but with a

⁶It has also been pointed out recently that this condition is not Renormalisation Group invariant [75].

\mathbb{Z}_2 discrete symmetry enforced,

$$\begin{aligned}
V_{\text{CW}}(\phi) = & \sum_{i \in h} n_i \frac{m_i^4(\phi, \xi_W, \xi_B)}{64\pi^2} \left[\log \left(\frac{m_i^2(\phi, \xi_W, \xi_B)}{Q^2} \right) - \frac{3}{2} \right] \\
& + \sum_{i \in V} n_i \frac{m_i^4(\phi)}{64\pi^2} \left[\log \left(\frac{m_i^2(\phi)}{Q^2} \right) - \frac{5}{6} \right] \\
& - \sum_{i \in f} n_i \frac{m_i^4(\phi)}{64\pi^2} \left[\log \left(\frac{m_i^2(\phi)}{Q^2} \right) - \frac{3}{2} \right],
\end{aligned} \tag{16}$$

$$V_T(\phi, T) = \frac{T^4}{2\pi^2} \left[\sum_{i \in h, V} n_i J_B \left(\frac{m_i^2(\phi, \xi_W, \xi_B)}{T^2} \right) + \sum_{i \in f} n_i J_F \left(\frac{m_i^2(\phi)}{T^2} \right) \right]. \tag{17}$$

In the above, the field-dependent fermion, Higgs and gauge boson masses take their usual form. There are two gauge-fixing parameters, ξ_W and ξ_B , that appear only implicitly through the masses of the mixed Goldstone-ghost scalars,⁷

$$m_{1,\pm}^2 = \frac{1}{2} \left(\chi \pm \text{Re} \sqrt{\chi^2 - \Upsilon_W} \right), \tag{18}$$

$$m_{2,\pm}^2 = \frac{1}{2} \left(\chi \pm \text{Re} \sqrt{\chi^2 - \Upsilon_Z} \right), \tag{19}$$

where

$$\chi = \frac{1}{\phi_h} \frac{\partial V_0}{\partial \phi_h} = -\mu_h^2 + \lambda_h \phi_h^2 + \frac{1}{2} \lambda_{hs} \phi_s^2, \tag{20}$$

and the gauge dependence appears only in the terms

$$\Upsilon_W = \chi g_2^2 \xi_W \phi_h^2 \quad \text{and} \quad \Upsilon_Z = \chi (g_2^2 \xi_W + g_1^2 \xi_B) \phi_h^2. \tag{21}$$

Because the Υ terms are proportional to the derivative of the tree-level potential, the ξ -dependence vanishes in the tree-level minima, as expected from Nielsen's identity. If $\Upsilon > 0$, by increasing ξ sufficiently it may be possible to make the square roots in eqs. (18) and (19) imaginary. As we take the real part, in this regime the potential would become independent of ξ .

The multiplicities for the Goldstone-like modes are $(n_1, n_2) = (2, 1)$ respectively to account for six terms in the effective potential, that is double the number of Goldstone modes. This is because the Goldstone and ghost contributions mix in the covariant gauge, so the total number of terms in the gauge-dependent effective potential is the same as in the R_ξ gauge. The positive and negative roots in eqs. (18) and (19) may both produce zero eigenvalues, potentially resulting in GC. The zeros occur in the tree-level vacuum, where $\Upsilon = \chi = 0$ for all ξ . For the negative roots, however, when $\xi = 0$ the zero eigenvalues are field-independent and so cannot contribute to the GC.

2.3 HT: The high-temperature approximation

The high-temperature (HT) approximation of the total effective potential is

$$V_{\text{HT}}(\phi, T) = V_0(\phi) + \frac{1}{2} c_h T^2 \phi_h^2 + \frac{1}{2} c_s T^2 \phi_s^2, \tag{22}$$

⁷They separate into Goldstone and ghost modes when $\xi = 0$.

where the Debye coefficients c_h and c_s are given in eqs. (45) and (46). At zero temperature, this reduces to the tree-level potential, $V_{\text{HT}}(\phi, T = 0) = V_0(\phi)$.

Equation (22) is obtained by considering only the leading terms of a high-temperature approximation of the finite-temperature correction in eq. (13). Namely, for $y \equiv m/T \ll 1$, the thermal functions are approximated by the leading terms in the expansions [80]

$$J_B(y^2) \simeq -\frac{\pi^4}{45} + \frac{\pi^2}{12}y^2, \quad (23)$$

$$J_F(y^2) \simeq \frac{7\pi^4}{360} - \frac{\pi^2}{24}y^2. \quad (24)$$

The zero-temperature Coleman-Weinberg corrections are neglected. Importantly, the gauge parameter ξ and renormalisation scale Q do not appear in this high-temperature expansion, leaving an explicitly gauge- and scale-independent high-temperature approximation to the potential. However, the fact that Q does not explicitly appear in the potential may in fact worsen the scale dependence, as explicit and implicit scale dependence are expected to partially cancel. The tadpole constraints are applied at tree-level, which avoids a potential source of gauge dependence.

In this scheme, the potential contains only quadratic and quartic terms, and the critical temperature and transition strength can be solved analytically,

$$T_c^2 = \frac{\lambda_h c_s \mu_s^2 - \lambda_s c_h \mu_h^2 - \sqrt{\lambda_h \lambda_s} |c_s \mu_h^2 - c_h \mu_s^2|}{\lambda_s c_h^2 - \lambda_h c_s^2}, \quad (25)$$

$$\gamma = \frac{1}{T_c} \sqrt{\frac{\mu_h^2 + \frac{1}{2} c_h T_c^2}{\lambda_h} + \frac{\mu_s^2 + \frac{1}{2} c_s T_c^2}{\lambda_s}}. \quad (26)$$

2.4 PRM: The \hbar expansion

This is a technique for computing the critical temperature and transition strength in a gauge-independent way [50]. The method exploits the Nielsen identity [81], which, when truncating the effective potential to one-loop, means that the one-loop effective potential is gauge independent at tree-level turning points. To maintain gauge independence, we ultimately use the tree-level, one-loop and high-temperature expansion of the effective potential in Sec. 2.3. As usual, the renormalisation scale enters explicitly in the Coleman-Weinberg potential and implicitly in the Lagrangian parameters.

We first find the minima of the tree-level potential, ϕ_{tree} . It is possible that the structure of minima in the tree-level potential does not match that of the one-loop potential. Therefore if there is only one minimum at tree-level, we further consider a saddle point. If there are no saddles, we consider a maximum. To ensure gauge independence of the critical temperature, the two points must be turning points.⁸ To ensure that no gauge dependence creeps into the tree-level potential, we fix Lagrangian parameters only using tree-level tadpoles and tree-level constraints on masses. To ensure the validity of Nielsen's identity, we cannot modify the field-dependent masses in the Coleman-Weinberg potential, even by terms that are formally order $\mathcal{O}(\hbar^2)$ or resum daisy terms by either the Parwani or Arnold-Espinosa methods.

⁸In our modified version of **PhaseTracer**, this choice is model-dependent and not automated.

We then turn to the one-loop potential with no daisy resummation. We find the temperature at which the two points considered are degenerate in the one-loop potential. This is the critical temperature, T_c . Lastly, at that critical temperature, we find the minima of the gauge-invariant high-temperature expansion of the potential, ϕ_{HT} . We use this in our estimate of the transition strength. For the strength of a transition involving one field that breaks electroweak symmetry,

$$\gamma_{\text{EW}} = \frac{|\phi_{\text{HT}}|}{T_c}. \quad (27)$$

In multi-field cases beyond our model, we would use the distance from ϕ_{HT} to the h -axis.

Importantly, because we use tree-level constraints and tadpoles to maintain gauge independence, we predict $v \simeq 246.22 \text{ GeV}$ and $m_h \simeq 125.25 \text{ GeV}$ only at tree-level. The most common approach for calculating the masses and observables in BSM theories to fix $v = 246.22 \text{ GeV}$ and use the loop corrected effective potential to fix parameters in the potential such that the minimum lies at $v = 246.22 \text{ GeV}$. In this way, one-loop tadpole diagrams vanish and do not need to be included in calculating observables. This is the approach implemented in most public tools, and therefore one needs to proceed with care when using the PRM method. The one-loop predictions for them could be quite different and disagree with measurements, and, depending on how they are computed, be gauge dependent. As we shall discuss, there is a risk that we are merely trading sensitivity to the choice of gauge for imprecision in agreement with experimental measurements; neither are desirable. Alternative approaches, such as the Fleischer–Jegerlehner treatment of tadpoles [82] may provide an approach to ensure that λ is extracted from the Higgs mass at the order \hbar without re-introducing gauge dependence into the effective potential (see also Ref. [83] for a recent discussion about the differences in these approaches). Later we study the impact of extracting λ_h at one loop by reintroducing gauge dependence via one-loop EWSB conditions and label this PRM + 1LHiggs_1LTad.

Lastly, we note that whilst the daisy treatments are an all-order resummation, and thus do not naturally fit into an \hbar -expansion scheme, Ref. [50] proposed a gauge-invariant modification to eq. (32) that could be incorporated into the PRM scheme. This method requires the effective three-dimensional theory and, as far as we know, is only rigorously proven to capture the $\mathcal{O}(\hbar^2 T^3)$ terms correctly. The conflict between IR divergences, which appear to require an all-order resummation, and the \hbar expansion is further discussed in Ref. [84].

2.5 OS-like: The on-shell-like scheme

The on-shell-like (OS-like) scheme is often used in studies of first-order phase transitions (see e.g. Ref. [39, 64, 85–89]). This scheme has the practical advantage that the tree-level VEVs and mass eigenstates are preserved at the one-loop level. That is, the masses extracted from the one-loop potential are the same as those extracted from the tree-level potential, and both potentials have a minimum at the same location in field space. Therefore in this work we compare results from the $\overline{\text{MS}}$ scheme and this OS-like scheme to indicate the differences in results that may be expected between the two most commonly used schemes.

Uncertainties from zero-temperature higher-order corrections are often estimated by comparing results in different renormalisation schemes. While both schemes can provide

controlled approximations allowing predictions that can be tested in experiments, the predictions will not in general be the same, with the difference coming from theoretical uncertainties arising from missing higher-order corrections in the respective schemes. Therefore, comparing the calculation in different schemes provides sensitivity to missing higher-order corrections and can be used as an estimate of this theoretical uncertainty.

Ref. [85] demonstrated that for field-dependent masses of the form

$$m^2(\phi) = m^2 + g\phi^2, \quad (28)$$

we may pick counter-terms that satisfy the OS conditions and bring the zero-temperature one-loop corrections in the Landau gauge into the simple form

$$V_{\text{CW}}(\phi) = \frac{1}{64\pi^2} \sum_i \tilde{n}_i \left[m_i^4(\phi) \left(\log \left(\frac{m_i^2(\phi)}{m_i^2(\mathbf{v})} \right) - \frac{3}{2} \right) + 2m_i^2(\mathbf{v})m_i^2(\phi) - \frac{1}{2}m_i^4(\mathbf{v}) \right], \quad (29)$$

where i ranges over the entire field-dependent mass spectrum (including scalars, gauge bosons and fermions), and we have defined $\tilde{n}_i \equiv (-1)^{2s_i}n_i$ to absorb the sign for particle species of spin s_i . The last term is field-independent and so is often ignored. The finite-temperature corrections are identical to those in Sec. 2.1.

We make a common simplification: we ignore the limitation eq. (28) and use eq. (29) in our SSM model with the field-dependent masses in appendix C. The OS conditions remain satisfied; however, eqs. (12) and (29) differ by terms that do not appear in the tree-level Lagrangian and cannot be interpreted as counter-terms. However, we predominantly consider transitions between ground states in which mixing between the Higgs and singlet vanishes, that is, between $(v_h(T), 0)$ and $(0, v_s(T))$ ground states. This potential is correct along these axes as the field-dependent masses are in the form eq. (28). See e.g. Ref. [32] for further discussion about implementing an OS-like scheme in scalar extensions of the SM.

3 Modifications to the effective potential

The treatments in Sec. 2 may be modified to alleviate the Goldstone catastrophe and resum daisy diagrams.

3.1 Goldstone catastrophe

The Goldstone catastrophe (GC) occurs when a massless goldstone boson entering loop functions leads to an infrared divergence. The GC should appear directly in the $\overline{\text{MS}}$ $\xi = 0$ potential at three-loop order and higher and in the electroweak symmetry breaking conditions at two-loop order and higher [70]. Furthermore it is very common in BSM physics investigations for the effective potential to be calculated using the effective potential approximation or OS-like schemes, and as discussed in Sec. 2 this causes the second derivative of the one-loop potential to diverge. For example, in the $\overline{\text{MS}}$ case this happens when the tree-level masses that appear in loop functions of the Coleman-Weinberg potential are fixed using a tree-level EWSB condition⁹, such that for $\xi = 0$ we have

⁹Note the EWSB constraints in eq. (6) are still applied at one-loop to fix the parameters appearing explicitly in the tree-level potential, here we just describe the standard treatment of tree-level $\overline{\text{MS}}$ masses that enter the loop functions.

massless Goldstone bosons. This particular issue could be avoided simply by relating the parameters to the Higgs pole masses with self energies evaluated with the momentum set equal to the Higgs mass [11] (see also Sec. 3.3 for comments on the impact of including the momentum), but here we consider instead two more direct alternatives that avoid the massless goldstone and could be used to avoid the GC appearing directly in the potential and electroweak symmetry breaking conditions:

1. **GC_SelfEnergy_Sol**: Adding the tree-level Goldstone boson mass with a one-loop self-energy correction to all Goldstone masses [69, 70]

$$M_{G^{0,\pm}}^2(\phi) = m_{G^{0,\pm}}^2(\phi) + \Sigma_G(\phi, p=0), \quad (30)$$

where the self energy contribution for the Goldstone can be given by,

$$\Sigma_G(\phi, p=0) = \frac{1}{\phi_h} \frac{\partial V'_{\text{CW}}}{\partial \phi_h}, \quad (31)$$

where V'_{CW} does not include Goldstone boson contributions. This correction depends on the renormalisation scale and gauge.¹⁰

2. **GC_Tadpole_Sol**: Applying EWSB constraints eq. (6) at one-loop when calculating the masses that enter the one-loop corrections to the potential.

In both cases this effectively adds a correction to the potential which is formally beyond the one-loop precision we aim for, while shifting the Goldstone masses away from the tree-level value. The former is formally re-summing a sub-class of corrections to all-orders, providing a principled solution (please see the extensive discussion in Refs. [69, 70] for details), while the latter is simply a convenient way to avoid the massless tree-level Goldstone that is easy to apply and done in the literature [64], while only introducing spurious two-loop pieces to the effective potential.

3.2 Daisy diagrams

There are two popular methods for resumming daisy diagrams:

1. Parwani [90]: This resums the finite-temperature daisy diagrams. To use the Parwani method, the mass eigenvalues appearing throughout the one-loop potential are replaced by thermal mass eigenvalues (see appendix C) and one forgoes the inclusion of any explicit daisy term. This has the well-known problem of producing effective linear terms that shift the high temperature vacuum away from the origin.
2. Arnold-Espinosa [91]: This resums only the zeroth Matsubara modes in the daisy diagrams. We add the daisy term

$$V_{\text{daisy}}(\phi, T) = -\frac{T}{12\pi} \sum_i \left[\left(\bar{m}_i^2(\phi, T) \right)^{3/2} - \left(m_i^2(\phi) \right)^{3/2} \right] \quad (32)$$

where $\bar{m}_i^2(\phi, T)$ are thermal masses including Debye corrections (see appendix C), and we have suppressed their gauge and scale dependence.

¹⁰We also apply this to the OS-like scheme and this introduces a renormalisation scale which we simply fix to ensure $d^2 V_{\text{CW}} / d\phi_h^2|_{\mathbf{v}} = (1/v_h) dV_{\text{CW}} / d\phi_h|_{\mathbf{v}}$.

Both methods introduce terms to the effective potential that are cubic in the coupling g for gauge bosons and to the $3/2$ power in scalar couplings. The thermal mass is, by contrast, quadratic in g and linear in scalar couplings. Neither treatment changes the zero-temperature potential. See Ref. [92, 93] for recent progresses about the two-loop order computations.

3.3 Renormalisation group equations

We take into account both the implicit and explicit scale dependence of the effective potential by using renormalisation group equations (RGEs) to run the $\overline{\text{MS}}$ parameters and compute the full $\overline{\text{MS}}$ renormalised effective potential. To do this we implement a **FlexibleSUSY** 2.6.1 [94, 95]¹¹ version of the effective potential in **PhaseTracer**. The **FlexibleSUSY** spectrum generator has two-loop RGEs, one-loop threshold corrections for the extraction of the gauge and Yukawa couplings and it also extracts the Higgs potential parameters using one-loop electroweak symmetry breaking conditions and one-loop self energies. The latter include the p^2 contributions, which are neglected when masses are calculated using the one-loop effective potential approximation. We have checked that it will lead to 1.3% difference on extracted λ_h and 1.0% difference on output T_c for benchmark point defined later in eq. (33). Due to the small size of this correction we do not consider it in our uncertainties. Since **FlexibleSUSY** uses the $\xi = 1$ gauge all the calculations using RGEs are fixed to that gauge and there are no Goldstone IR divergences for this choice. The inputs of the **FlexibleSUSY** model file are m_h , m_s , λ_s and λ_{hs} , while λ_h , μ_h and μ_s are determined by EWSB conditions.

4 Results

We now investigate different sources of uncertainty in the analysis of a PT, including gauge dependence, renormalisation scale dependence, treatment of the Goldstone catastrophe (GC), resummation of daisy diagrams, and renormalisation schemes. We do so by applying the treatments discussed in Secs. 2 and 3 to the SSM. After considering them separately, we compare their typical sizes across the available parameter space. The numerical uncertainties associated with our computational methods are discussed in appendix D.

4.1 Gauge dependence

4.1.1 Benchmark point

First, in Fig. 2 we show the ξ -dependence of the critical temperature T_c and transition strength γ_{EW} in the R_ξ and covariant gauges for different methods, using a benchmark point of

$$\lambda_s = 0.1, \quad \lambda_{hs} = 0.3 \quad \text{and} \quad m_s = 65 \text{ GeV}. \quad (33)$$

This benchmark lies near the center of the region of parameter space in which a FOPT could occur. We vary the gauge parameter between $\xi = 0$ and 60. Note that the upper

¹¹**FlexibleSUSY** uses **SARAH** 4.14.3 [96–99] and parts of the **SOFTSUSY** [100, 101] code.

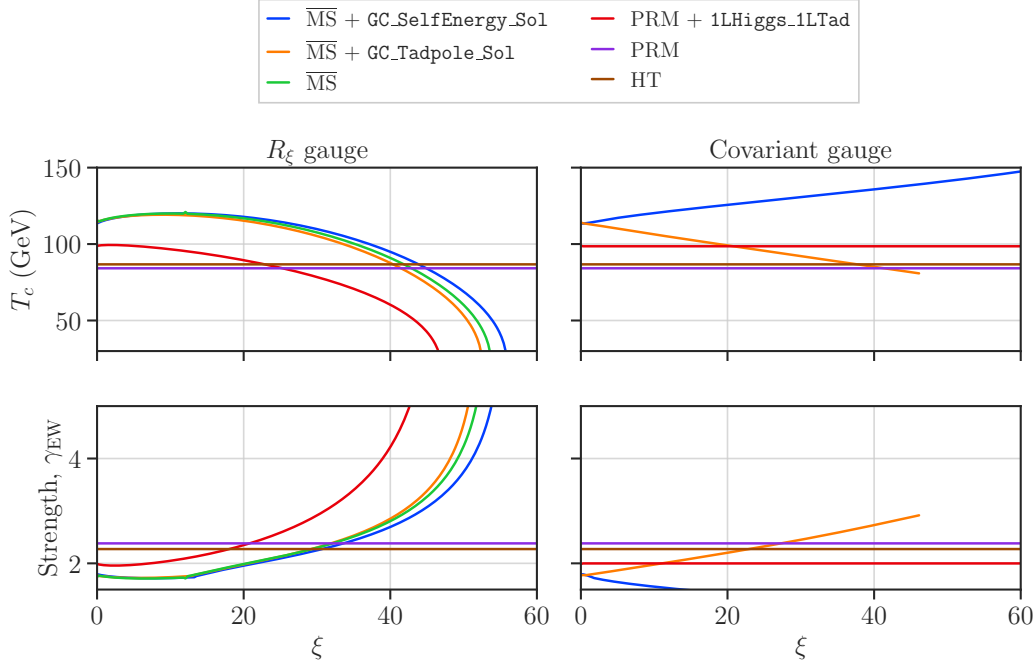


Figure 2: The gauge dependence from different methods for the critical temperature (top) and transition strength (bottom) in R_ξ (left) and covariant gauge (right) for the benchmark point in eq. (33).

limit may lie beyond constraints from perturbativity [61, 76], as increasing the gauge parameter aggravates IR divergences that spoil perturbation theory. The legend follows the notation introduced in Secs. 2 and 3. In the three $\overline{\text{MS}}$ methods, we used the Arnold-Espinosa technique to resum daisy terms, and set $Q = m_t$. The gauge dependence of the OS-like scheme is not presented as eq. (29) is only valid at $\xi = 0$.

As a reference, in Fig. 2 we show the PRM and HT methods which, of course, are independent of the gauge parameter ξ . The left panels of Fig. 2 show results for the R_ξ gauge. In the $\overline{\text{MS}}$ scheme, with ξ increasing, the critical temperature T_c increases slightly for small values of ξ , and then decreases significantly for large values of ξ . With ξ increasing even further, there is no FOPT for this benchmark point anymore in the gauge-dependent schemes. The choice of treatment of the GC has limited impact.

In Fig. 2 we investigated $\xi \leq 60$. However, there may be constraints on perturbativity that impose $\xi \lesssim 1$ [61, 76]. We see in Fig. 3 that varying the gauge between $\xi = 0$ and 1 results in only slight changes in the properties of the FOPT. We furthermore see that some methods do not depend smoothly on ξ . For example, the T_c of $\overline{\text{MS}}$ blows up at $\xi = 0$. This originates from the GC: due to the catastrophe, the second-derivatives of the one-loop potential are singular, and so the Lagrangian parameters required in the tree-level potential to maintain finite scalar masses diverge. Although using the modified μ from one-loop tadpole cures the GC at $\xi = 0$, the Goldstone may be massless at tree-level in the one-loop vacuum for other values of ξ . For this benchmark point, when $\xi = 0$, $M_{G^0}^2 \simeq M_{G^\pm}^2 \simeq -840 \text{ GeV}^2$; when $\xi = 0.0995$, $M_{G^0}^2 \simeq 0 \text{ GeV}^2$ and $M_{G^\pm}^2 \simeq -200 \text{ GeV}^2$; when $\xi = 0.1286$, $M_{G^0}^2 \simeq 250 \text{ GeV}^2$ and $M_{G^\pm}^2 \simeq 0 \text{ GeV}^2$. This is why we see two singularities

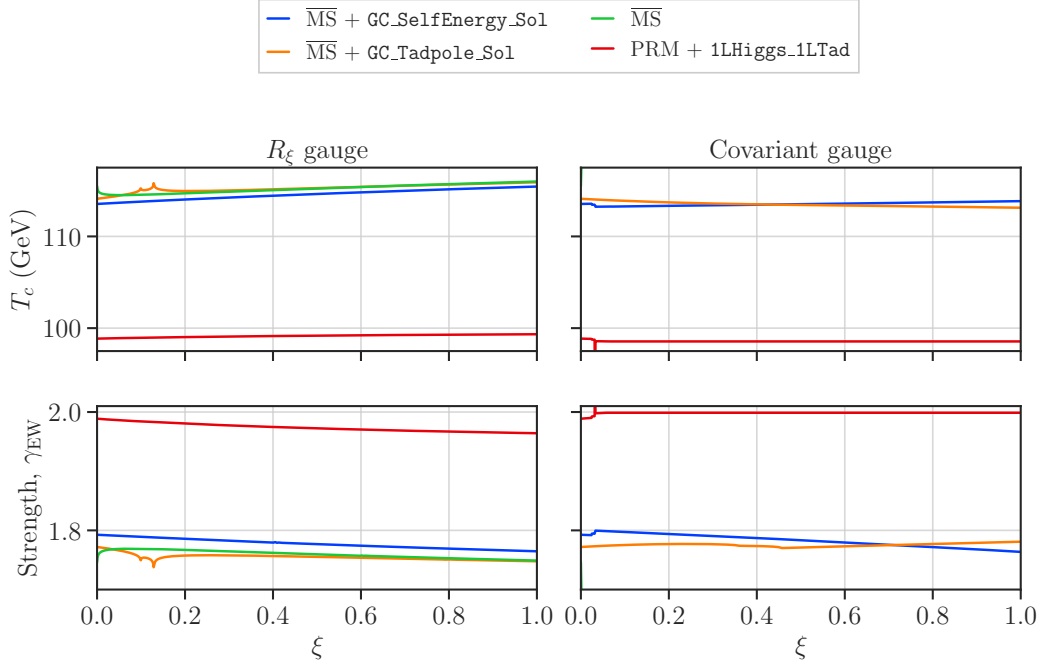


Figure 3: As per Fig. 2, but for $\xi \leq 1$. Lines for PRM and HT are not shown here, as they are independent of ξ and exactly the same as in Fig. 2.

(zeros) in the T_c (γ_{EW}) of the orange curve for $\overline{\text{MS}} + \text{GC_Tadpole_Sol}$ at $\xi \simeq 0.1$ and $\xi \simeq 0.13$. The catastrophe could occur at other ξ for other choices of benchmark point. In contrast, adding the one-loop self-energy to the Goldstone masses avoids a catastrophe at any ξ as seen in the blue curve for $\overline{\text{MS}} + \text{GC_SelfEnergy_Sol}$.

In $\text{PRM} + 1\text{LHiggs_1LTad}$, we use one-loop tadpole conditions to set the Lagrangian parameter μ_h and extract λ_h and μ_s at the one-loop level from the measured Higgs pole mass and the input singlet pole mass, respectively. The one-loop tadpoles are required if one wants to extract λ_h from the Higgs mass at the one-loop level using the standard approach we applied in the $\overline{\text{MS}}$ calculation, where the tadpoles vanish in the mass corrections and do not need to be explicitly included¹². A one-loop extraction of λ_h is required for a consistent order \hbar calculation of the effective potential consistent with the measured Higgs pole mass. As a result, the T_c and γ_{EW} calculations in this method are closer in spirit to those in the $\overline{\text{MS}}$ method and numerically are closer when far away from the ξ values where the $\overline{\text{MS}}$ and pure PRM results match. This, however, introduces gauge dependence, which contradicts the purpose of the PRM method. This gauge dependence originates from the gauge dependence of the $\overline{\text{MS}}$ scalar masses (which are extracted at the one-loop level) used in the one-loop tadpole conditions. Just as in the $\overline{\text{MS}}$ scheme, however, T_c significantly changes with increasing ξ for this case at this benchmark point.

We show results in the covariant gauge in the right panels of Figs. 2 and 3, where $\xi \equiv \xi_B = \xi_W$. As anticipated, results from the covariant and R_ξ gauges are identical at $\xi = 0$. The results for the $\overline{\text{MS}}$ calculation without any modification to solve the GC

¹²Though they must be accounted for if you use the tree-level EWSB condition to rewrite the tree-level Higgs mass as $\overline{m}_h = \sqrt{2\lambda}v$.

cannot be seen as the GC exists for all ξ in the covariant gauge.

Different to the R_ξ gauge, in the covariant gauge the T_c for $\overline{\text{MS}} + \text{GC_SelfEnergy_Sol}$ and $+ \text{GC_Tadpole_Sol}$ respectively increase and decrease almost linearly with ξ increasing. Meanwhile, there are some discontinuities in the lines of the covariant gauge when ξ is small, while the lines then become continuous when ξ is large. This is because we take the real part of the square root in eqs. (18) and (19) and for sufficiently large ξ , the ξ -dependent parts are imaginary. This behavior can also be seen in the results of PRM $+ 1\text{LHiggs_1LTad}$ in the covariant gauge, i.e. there are two steps in the results at small ξ and the results are independent of ξ for large ξ . This gauge independence, however, does not necessarily mean that this method is a better choice, because it is simply due to the fact that we ignored the imaginary gauge-dependent parts of the squared masses. There are no results when $\xi > 46.5$ for $\overline{\text{MS}} + \text{GC_Tadpole_Sol}$ because our iterative solver for λ_h using one-loop EWSB did not converge. The gauge dependence of the $\overline{\text{MS}} + \text{GC_SelfEnergy_Sol}$ in the covariant gauge is also fairly strong, though it shows a different tendency.

The gauge dependence in the calculations of T_c and γ_{EW} originates from two sources: indirectly from the Lagrangian parameters chosen by solving one-loop tadpole conditions and explicitly in the one-loop potential. The indirect dependence causes T_c to decrease with increasing ξ , as shown by the PRM $+ 1\text{LHiggs_1LTad}$ results in R_ξ gauge, which only suffers from this source. The explicit dependence, on the other hand, increases T_c , as shown by the $\overline{\text{MS}} + \text{GC_SelfEnergy_Sol}$ results in the covariant gauge with large ξ . In this case, the ξ dependence vanishes in the zero-temperature vacuum, as the square roots in eqs. (18) and (19) are imaginary, such that the tadpoles are gauge independent. However, the potential remains gauge dependent at other field values. When both contributions appear at the same time, such as in the $\overline{\text{MS}}$ scheme with the R_ξ gauge and the $\overline{\text{MS}} + \text{GC_Tadpole_Sol}$ in the covariant gauge, the indirect dependence through tadpoles overpowers the explicit dependence.

4.1.2 Two-dimensional scans

The above discussion is based on a single benchmark point. The magnitude of the gauge dependence, however, may depend strongly on the Lagrangian parameters. In Fig. 4, we show the uncertainty from the choice of gauge parameter in the $\overline{\text{MS}} + \text{GC_SelfEnergy_Sol}$ prediction for the critical temperature T_c with three two-dimensional scans of the Lagrangian parameters. We quantify this uncertainty through

$$\Delta_\xi T_c \equiv |T_c(\xi = 0) - T_c(\xi = 25)|, \quad (34)$$

where $T_c(\xi = 0, 25)$ is the critical temperature with $\xi = 0, 25$ in the $\overline{\text{MS}} + \text{GC_SelfEnergy_Sol}$ scheme. As discussed in the introduction, this quantification is somewhat arbitrary. We attempted to pick an upper limit, $\xi = 25$, that strikes a balance between understating the uncertainty and constraints from perturbativity. If we were to increase the upper limit further, eventually there would be no points with FOPT simultaneously at $\xi = 0$ and the upper limit. We scan over two of the three free parameters, while fixing m_s , λ_{hs} and λ_s to their values in eq. (33) in the left, middle and right panels, respectively. To help understand the gauge dependence further, we show $T_c(\xi = 0)$ in the lower panels.

We found no valid points in the blank regions of Fig. 4. The causes for this and the phase structures of points in those regions are discussed in appendix A. In the colored

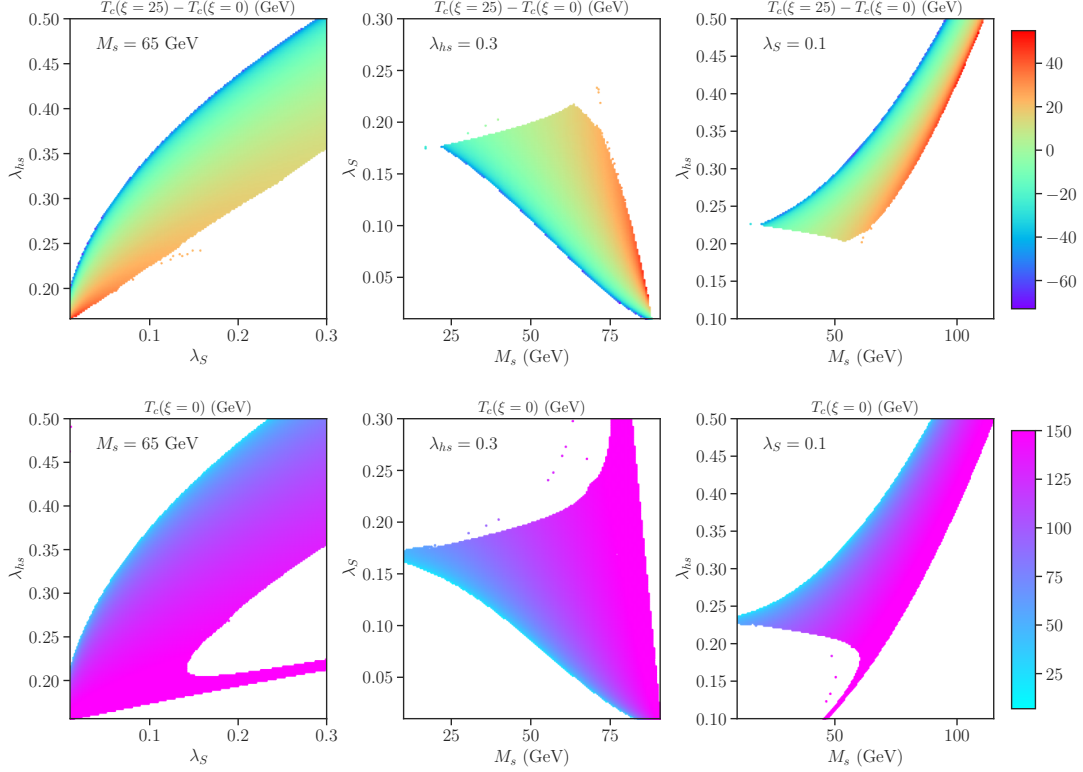


Figure 4: Gauge-dependence of the $\overline{\text{MS}} + \text{GC.SelfEnergy.Sol}$ scheme for the critical temperature T_c in two-dimensional scans. We use the difference in eq. (34) between $\xi = 0$ and 25 to show the gauge-dependence in the upper panels. We show the corresponding $T_c(\xi = 0)$ displayed in the lower panels. In the blank regions there are no points with a FOPT at $\xi = 0$ and $\xi = 25$.

regions, the critical temperature changes with the varying input parameters. The trends can be derived from the expression of T_c in the high-temperature approximation, eq. (25). Alternatively, consider the two minima at temperature T , $\phi_s(T) \equiv (v_h^{\text{high}} = 0, v_s^{\text{high}}(T))$ and $\phi_h(T) \equiv (v_h^{\text{low}}(T), v_s^{\text{low}} = 0)$. We may Taylor expand the difference in potential around $T = 0$ [23, 102]

$$\Delta V(T = T_c) \approx \Delta V(T = 0) + T_c \left. \frac{\partial \Delta V}{\partial T} \right|_{T=0}, \quad (35)$$

where $\Delta V(T) \equiv V(\phi_s(T), T) - V(\phi_h(T), T)$. Since this difference vanishes at the critical temperature and $\Delta V(T = 0) < 0$, we find

$$T_c \approx - \frac{\Delta V(T = 0)}{\left. \frac{\partial \Delta V}{\partial T} \right|_{T=0}}. \quad (36)$$

Accordingly, a smaller gap at zero temperature may imply a lower T_c . In the SSM at tree level we have

$$\Delta V(T = 0) = -\frac{1}{4} \frac{\mu_s^4}{\lambda_s} + \frac{1}{4} \frac{\mu_h^4}{\lambda_h} \approx -\frac{1}{4} \frac{(\frac{1}{2} \lambda_{hs} v_h^2 - m_s^2)^2}{\lambda_s} + \frac{1}{8} m_h^2 v_h^2, \quad (37)$$

where $\frac{1}{2}\lambda_{hs}v_h^2 > m_s^2$. We can approximately infer that with increasing λ_s and m_s , and decreasing λ_{hs} , the gap $\Delta V(T=0)$ and thus T_c must increase. This agrees with the lower panels of Fig. 4.

In the upper panels of Fig. 4, we show the uncertainty in T_c caused by changing the gauge parameter ξ in the regions in which a FOPT could occur for both $\xi = 0$ and $\xi = 25$. The change $\Delta_\xi T_c$ varies from -73 GeV to $+55$ GeV, and increases smoothly with λ_{hs} decreasing, m_s increasing and λ_s increasing. In Appendix B we also provide Tab. 2 which shows precise input parameters and the output critical temperatures of the benchmark point in eq. (33) and points around it for $\xi = 0$ and $\xi = 25$, to give quantitative results that also show the trends discussed here.

4.2 Renormalisation scale dependence

The renormalisation scale dependence of the PT properties originates from the scale-dependence of the one-loop corrections to the effective potential. If RGEs are used, this may be partly balanced by renormalisation-scale dependence of the Lagrangian parameters. In this work, we run the Lagrangian parameters to different scales using **Flexible-SUSY**, which uses the $\overline{\text{MS}}$ scheme with $\xi = 1$ by default. We do not consider the OS-like scheme in this section, since there is no free renormalisation scale to vary for that method.

4.2.1 Benchmark point

In Fig. 5, we show the renormalisation scale dependence in the $\overline{\text{MS}}$ scheme and PRM methods, by varying the renormalisation scale from $Q = \frac{1}{2}m_t$ to $Q = 2m_t$. We choose this interval because it is expected to capture uncertainty from the most important missing high-order corrections from the top quark at $T = 0$. Here we use the one-loop resummed Goldstone mass to treat the GC and the Arnold-Espinosa method to resum Daisy terms. In each of the panels, we vary one input parameter around the benchmark point in eq. (33). The top and bottom two rows of panels in Fig. 5 show the uncertainties on T_c and γ_{EW} , respectively. The lower edge, center, and upper edge of the bands in the first and third rows indicate results at $Q = \frac{1}{2}m_t$, m_t , and $2m_t$, respectively. To highlight the uncertainties, we separately show the fractional changes, $(T_c(Q = \frac{1}{2}m_t) - T_c(Q = 2m_t))/T_c(Q = m_t)$ and $(\gamma(Q = \frac{1}{2}m_t) - \gamma(Q = 2m_t))/\gamma(Q = m_t)$, directly by colored lines in the second and fourth rows of panels.

We see almost no parameter dependence in the results at $\lambda_{hs} \lesssim 0.2$ and $m_s \gtrsim 90$ GeV. In these regions the transition is between $(\phi_h = 0, \phi_s = 0)$ and $(\phi_h \neq 0, \phi_s = 0)$ and thus is independent of parameters related to the singlet. In the bottom right panel, $\Delta_Q \gamma / \gamma$ of $\overline{\text{MS}}$ scheme with Parwani method suddenly flips sign at $m_s = 84.67$ GeV, which is caused by a numerical issue. The T_c of this point is near to the end temperature of one phase, so the potential around the corresponding minimum at T_c are rather flat, which lead to large uncertainty for local minimum finding algorithm. For detailed discussion about numerical uncertainties, see appendix D. Unlike Ref. [103], we show PRM results even if the high-temperature approximation of the effective potential contained a single minimum at the critical temperature. For $\lambda_s \approx 0.15$, that single minima was at the origin for $Q = \frac{1}{2}m_t$ leading to $\gamma_{\text{EW}} = 0$. The change in T_c for the PRM methods is typically mild and less than about 10%, though γ_{EW} shows more sensitivity, typically less than

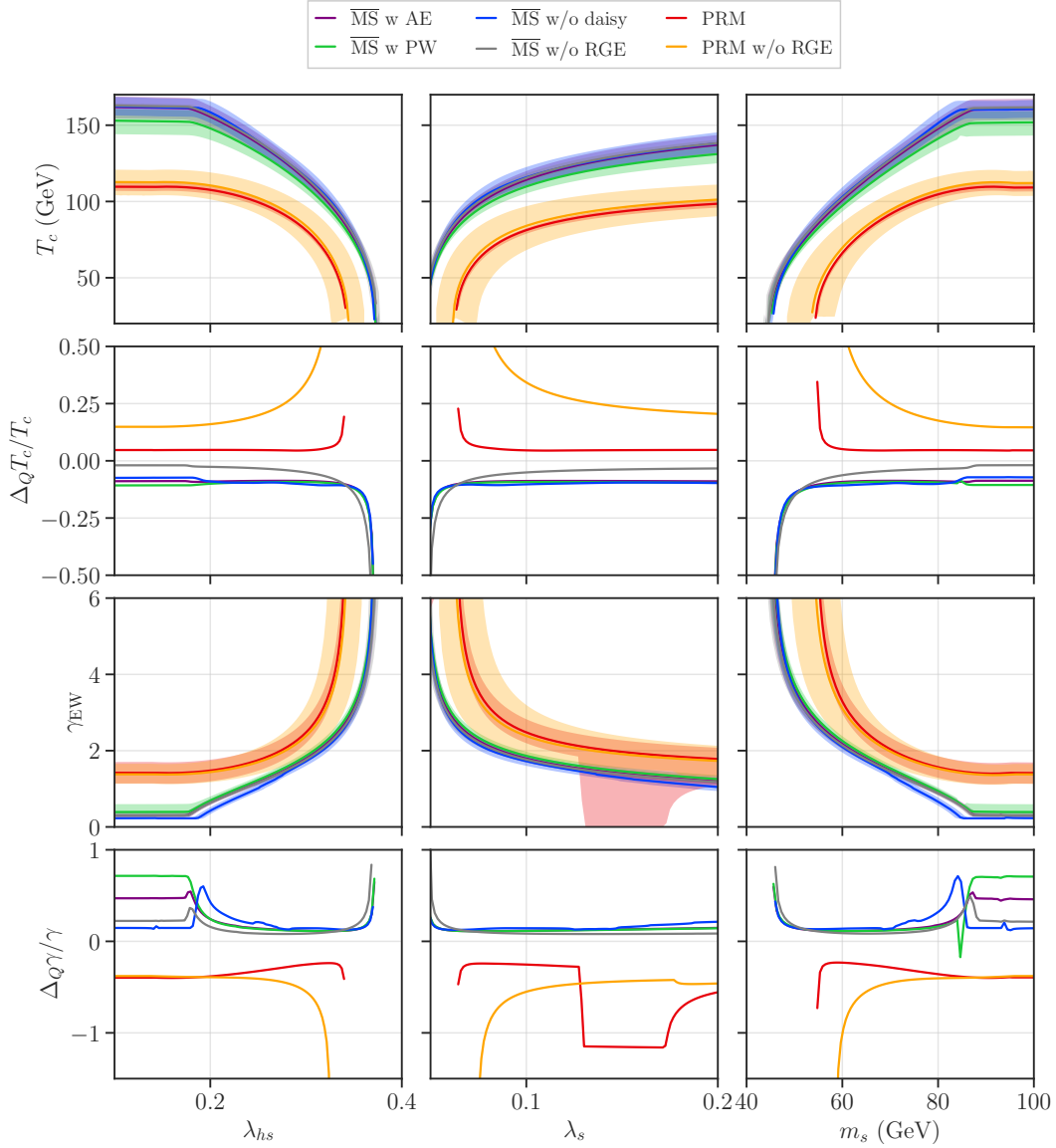


Figure 5: The renormalisation scale dependence in the $\overline{\text{MS}}$ scheme and PRM method found by varying the renormalisation scale from $Q = \frac{1}{2}m_t$ to $2m_t$. In each of the columns, we vary one input parameter of the benchmark point in eq. (33). The lower edges, center and upper edges of the bands in the first and third rows show the T_c and γ_{EW} at $Q = \frac{1}{2}m_t, m_t$, and $2m_t$ separately. The second and last rows show the fractional change in T_c and γ_{EW} , respectively. The labels ‘w AE’, ‘w PW’ and ‘w/o daisy’ indicate daisy resummation with the Arnold-Espinosa method, the Parwani method, and no resummation, respectively.

about 20%.

A common and important feature in all the results, however, is that the uncertainties rise sharply when the critical temperature is sensitive to the Lagrangian parameters. This is not only true for the uncertainty caused by scale dependence, but also true for

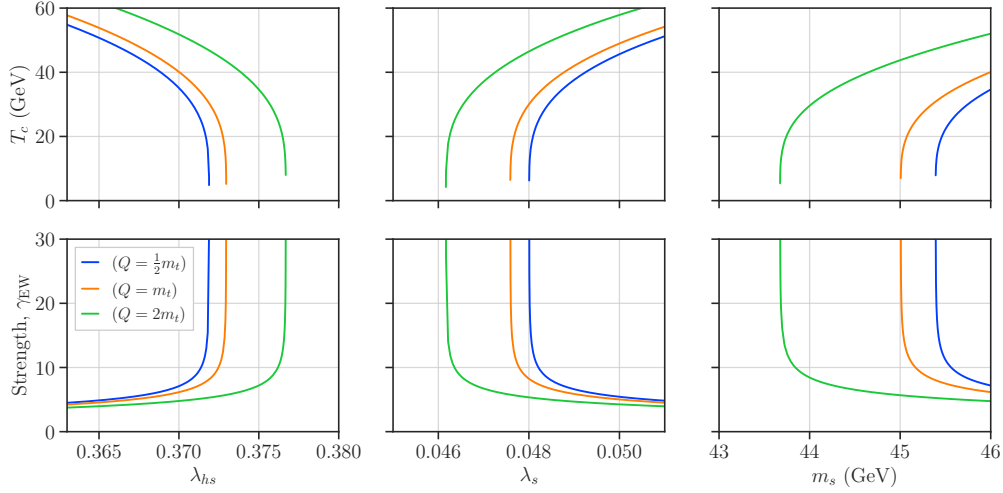


Figure 6: Similar to Fig. 5 though for $T_c \lesssim 60$ GeV, and only results for the $\overline{\text{MS}}$ scheme with AE are shown by colored lines.

the uncertainty caused by gauge dependence discussed in the above subsection, and the uncertainties presented in the following subsection. As the variation of renormalisation scale or gauge parameter slightly changes the Lagrangian parameters, it is obvious that when the critical temperature is sensitive to the parameters, the critical temperature and transition strength become sensitive to the renormalisation scale or gauge parameter. This happens in the region of large λ_{hs} , small λ_s and small m_s , where the critical temperature is relatively small. There are no results for $T_c < 30$ GeV in Fig. 5 because we find points in the plots by a grid scan of the parameters, and the grid misses fine-tuned cases in which $T_c < 30$ GeV. To find results in that region we performing a more detailed scan in a smaller parameter range where we expect to find smaller T_c . We show the $\overline{\text{MS}}$ result for the resulting low temperature range in Fig. 6. To obtain $T_c < 5$ GeV, the parameters have to be tuned to one part in 10^7 . The reason can be seen from eq. (37). A zero critical temperature means no energy gap between the EW VEV in the ϕ_h direction and a local minimum on ϕ_s direction, so the parameters should cancel each other.

With RGE running and the Parwani method, the scale uncertainties in the $\overline{\text{MS}}$ result for T_c are about 16 GeV for $T_c \approx 150$ GeV. As T_c decreases, the relative uncertainty changes from approximately constant to sharply increasing in magnitude at $T_c < 40$ GeV. Using the Arnold-Espinosa method or eliminating daisy resummation results in similar uncertainties with the same tendency. When $T_c \lesssim 20$ GeV, the daisy corrections, which are proportional to the temperature T^4 (see eq. (32)), are negligible. Consequently, in this regime the scale dependence of different treatments of daisy resummation are approximately the same.

We see that $\Delta_Q T_c$ of the $\overline{\text{MS}}$ scheme without RGE running is smaller than the one with RGE running, which is counter-intuitive. For example at leading order there are

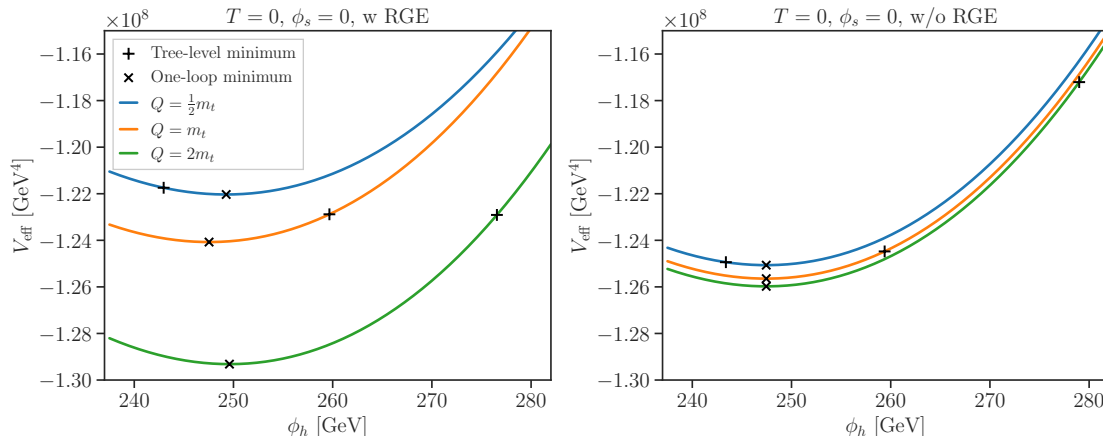


Figure 7: The zero-temperature effective potential in the $\overline{\text{MS}}$ scheme for the benchmark point in eq. (33) at different renormalisation scales, with (left) and without RGE running (right).

cancellations such that¹³ [66]

$$\mu \frac{d}{d\mu} (V_0 + V_{\text{CW}}) = 0 \quad (38)$$

and there can be further cancellations of scale dependence in the temperature-dependent parts of the potential. In the Parwani method, scale dependence in finite-temperature bosonic contributions cancels scale dependence in temperature-dependent terms introduced in the CW potential by the Parwani method. The cancellation eq. (38) is, however, spoilt by next-to-leading order terms, such as two-loop running of parameters in the tree-level potential and one-loop running of parameters in the CW potential, and in general requires that we consider the β -functions for all Lagrangian parameters and the anomalous dimensions of the fields. In our calculation, we apply two-loop RGEs and omit the anomalous dimension, such that eq. (38) no longer holds exactly. Furthermore, we include finite-temperature corrections from the top quark, and the scale cancellations in the Parwani method only occur for bosonic corrections. Consequently, results that include RGE running suffer from greater scale uncertainties than results without RGE running, and the Parwani method makes the situation even worse. This is somewhat counter-intuitive, as the derivative of the Parwani improved Coleman Weinberg potential with respect to the RG scale has terms that are quadratic in temperature and negative in sign, so one might expect they naively cancel the scale dependence of the quadratic contribution to the thermal functions. However, the combined β function for the thermal mass turns out to be negative as it is dominated by top quark interactions. So the new scale-dependent contribution in Parwani adds to, rather than cancels, the scale dependence of the un-resummed theory.

In Fig. 7, we display the zero-temperature potentials of the $\overline{\text{MS}}$ scheme with the Arnold-Espinosa method for the benchmark point of $\lambda_s = 0.1$, $\lambda_{hs} = 0.3$ and $m_s = 65$ GeV. We can see clearly that eq. (38) does not hold with RGE running in our calcula-

¹³Note that the left-hand side in eq. (38) includes contributions from wavefunction renormalisation, $-\gamma_\phi \phi \frac{dV}{d\phi}$ where γ_ϕ here is the anomalous dimension, as well as contributions from the β functions for the Lagrangian parameters.

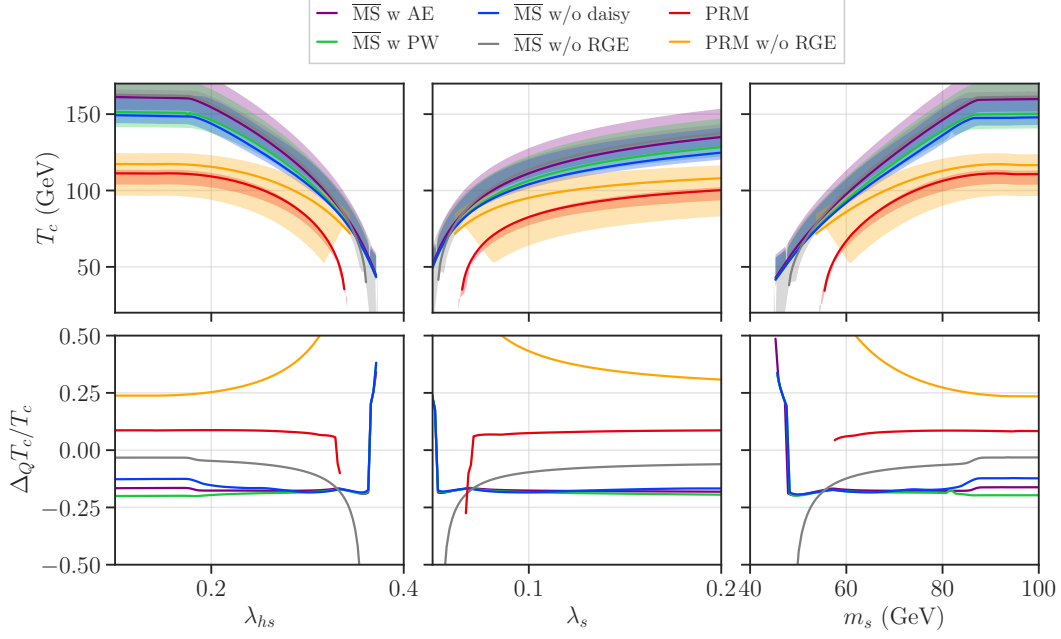


Figure 8: Similar to Fig. 5, but for the renormalisation scale dependence in the $\overline{\text{MS}}$ scheme and PRM method found by varying the renormalisation scale from $Q = T/2$ to $2\pi T$ by solving eq. (39).

tion, and that the potential suffers from greater scale dependence when we include RGE running. We also mark the tree-level minimum since the PRM method evaluates the one-loop potential at the minima of the tree-level potential. Fig. 7 shows that changes in the one-loop potential at the tree-level minima with RGE running are smaller than that without RGE running, as with RGE running the tree-level minima approximately lie on a horizontal line of constant potential. Therefore, the $\Delta_Q T_c$ for the PRM method with RGE running is smaller than $\Delta_Q T_c$ without RGE running. Note that for the PRM method, $T_c(Q = \frac{1}{2}m_t) > T_c(Q = 2m_t)$.

Fig. 5 shows that $\Delta_Q T_c$ of the PRM method with RGE running is rather small and roughly independent of Lagrangian parameters, typically about 5% for T_c , though it can exceed about 20% for very small critical temperatures. Without RGE running, $\Delta_Q T_c$ can be larger than 15%, and increases rapidly with T_c decreasing. This implies that proper RGE running is quite essential in the PRM method to reduce the renormalisation scale dependence. Looking only at $\Delta_Q T_c$, the $\overline{\text{MS}}$ scheme has larger scale uncertainties than the PRM method, but considering $\Delta_Q \gamma$, the $\overline{\text{MS}}$ scheme has smaller scale uncertainties than the PRM method. The increased uncertainty in γ in the PRM method may be connected to the fact that the numerator, $\Delta\phi_h$, and denominator, T_c , are obtained from two different potentials in this method.

Finally, we consider a broader variation of the renormalisation scale from $Q = T/2$ to $2\pi T$. This interval was chosen to capture uncertainty from missing higher-order corrections at finite temperature, specifically involving the soft scale $\sim gT$ and the first Matsubara mode as discussed in Ref. [65]. Here, the renormalisation scale changes throughout a calculation, as whenever the potential is evaluated at a temperature T , the renormalisation scale is set to a scale $Q \propto T$. We perform calculations at $Q = T$, $Q = T/2$ and

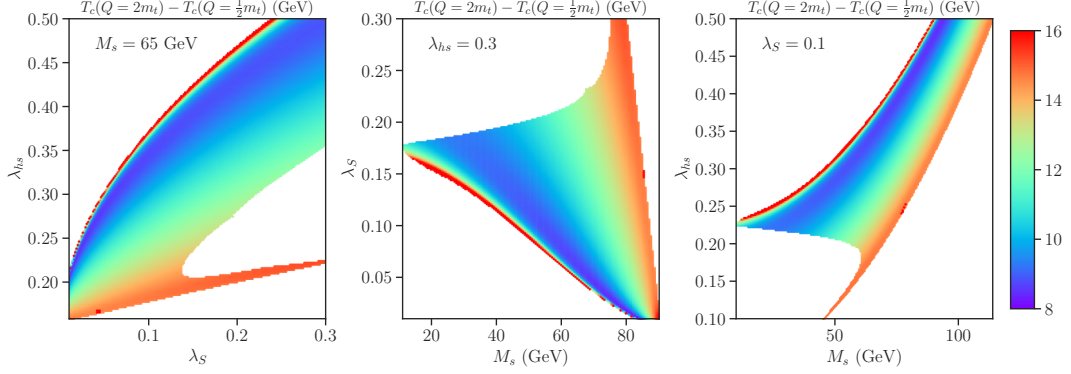


Figure 9: The renormalisation scale dependence in the $\overline{\text{MS}}$ scheme for the critical temperature T_c found by varying the renormalisation scale from $Q = \frac{1}{2}m_t$ to $2m_t$ in 2-dimensional scans. In the blank regions there are no points with a FOPT at both $Q = \frac{1}{2}m_t$ and $2m_t$. We fix $m_s = 62.5$ GeV in the left panel, $\lambda_{hs} = 0.3$ in the middle panel, and $\lambda_s = 0.1$ in the right panel.

$Q = 2\pi T$ by solving the following equations iteratively for T ,

$$T_c(Q = T) = T, \quad T_c(Q = T/2) = T, \quad T_c(Q = 2\pi T) = T. \quad (39)$$

By doing so, we ensure that at temperature $T = T_c$ the potential was computed at the renormalisation scales $Q = T/2$, T and $2\pi T$, as required. We show the variation in the critical temperature in Fig. 8. We see that the uncertainty bands are broader compared to Fig. 5, especially for the PRM method for which the relative uncertainty was always greater than about 25%. The $\Delta_Q T_c / T_c$ of $\overline{\text{MS}}$ scheme flips sign and shoots up at low T_c . With scale Q fixed by eq. (39), T_c also decreases with λ_{hs} increasing, or λ_s and m_s decreasing. The slope of T_c against the input parameters is larger when $Q = 2\pi T$ than when $Q = T/2$, especially for low T_c . Thus the uncertainty flips sign at certain value of T_c .

4.2.2 Two-dimensional scans

We now turn to two-dimensional planes of the SSM parameters to check the renormalisation scale dependence throughout the model's parameter space. Here we change the scale using RGE running, use the $\overline{\text{MS}}$ scheme and the R_ξ gauge, and include daisy corrections. In Fig. 9, we show the difference of critical temperature $\Delta_Q T_c = |T_c(Q = \frac{1}{2}m_t) - T_c(Q = 2m_t)|$ on the λ_s - λ_{hs} , m_s - λ_s and m_s - λ_{hs} planes. The colored regions are obtained by two-dimensional scans with $m_s = 62.5$ GeV fixed in the left panel, $\lambda_{hs} = 0.3$ fixed in the middle panel, and $\lambda_s = 0.1$ fixed in the right panel. In the blank regions there were no points with a FOPT at both $Q = \frac{1}{2}m_t$ and $Q = 2m_t$.

The tendency exhibited in the two-dimensional planes in Fig. 9 is consistent with that in the one-dimensional results. The uncertainties at first decrease with λ_{hs} increasing, λ_s decreasing and m_s decreasing, but subsequently rise sharply. In most of the parameter space, the uncertainties lie around 8 GeV – 16 GeV. The magnitude of the uncertainties can reach more than 50 GeV when $T_c < 60$ GeV (see Fig. 6). The maximum value of ΔT_c is dependent on the resolution of the scan. With two-dimensional grid scans of 200 points per dimension in the ranges $0.1 < \lambda_{hs} < 0.5$, $0.01 < \lambda_{hs} < 0.3$ and $10 \text{ GeV} <$

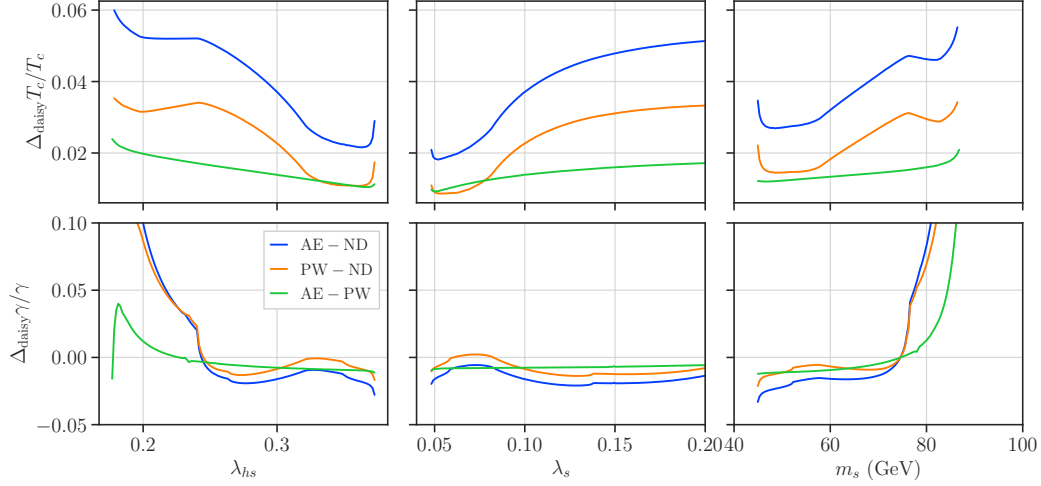


Figure 10: Differences in critical temperature and transition strength with different methods for resummation of daisy diagrams, in the $\overline{\text{MS}}$ scheme of $\xi = 0$ and $Q = m_t$. ‘PW’ and ‘AE’ stand for adding daisy resummation using the Parwani method and the Arnold-Espinosa method respectively, while ‘ND’ indicates no resummation of daisy diagrams. In each of the panels we vary one input parameter about the benchmark point in eq. (33).

$m_s < 120$ GeV, we found a maximum ΔT_c of 40.2 GeV at the parameter point $\lambda_{hs} = 0.43$, $\lambda_s = 0.1$, $m_s = 76.9$ GeV, $T_c(Q = \frac{1}{2}m_t) = 6.2$ GeV and $T_c(Q = 2m_t) = 46.4$ GeV.

4.3 Daisy resummation dependence

In Fig. 10, we present differences in T_c and γ_{EW} with different treatments of daisy diagrams — the Parwani method and the Arnold-Espinosa method described in Sec. 3.2, and discarding resummation of daisy diagrams. We can see that in the SSM the effects of daisy resummation on transition properties are relatively small (though this effect may be bigger in other models; see e.g. Ref. [11, 32, 104]).

The changes in T_c caused by switching between the Parwani and the Arnold-Espinosa methods are less than 3% and the changes caused by switching off daisy resummation altogether were less than 6%. The changes decrease with λ_{hs} increasing or λ_s and m_s decreasing, which means T_c decreasing (see top panels of Fig. 11). Unlike changes caused by varying the gauge parameter or renormalisation scale, varying the treatment for daisy resummation does not alter the Lagrangian parameters. Therefore, here the changes in T_c do not rise sharply at low T_c . On the other hand, the relative changes in γ_{EW} are typically even smaller, but increase rapidly for large T_c , simply because that γ_{EW} are very small. The absolute changes in γ_{EW} are less than 0.06 when $T_c > 100$ GeV and $\gamma_{EW} < 0.4$.

4.4 Comparison of renormalisation schemes and other methods

We now turn to the renormalisation schemes. In Fig. 11, we compare results of the $\overline{\text{MS}}$ and OS-like scheme, together with the high temperature approximation which is

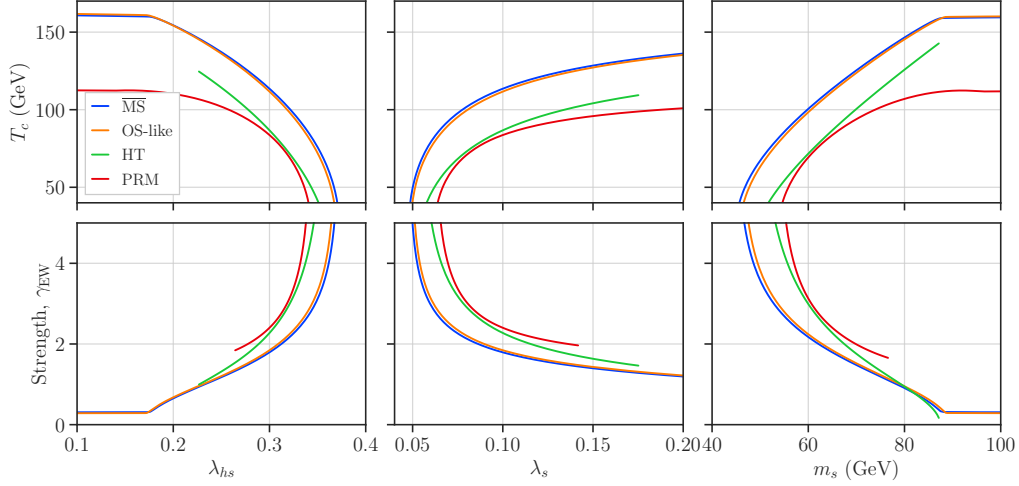


Figure 11: Critical temperature and transition strength in the $\overline{\text{MS}}$ scheme, OS-like scheme, HT approximation, and PRM method. The other settings ($\xi = 0$, $Q = m_t$, using Arnold-Espinosa method and `GC_SelfEnergy_Sol`) are the same if they are optional in that scheme. In each of the panels we vary one input parameter about the benchmark point in eq. (33).

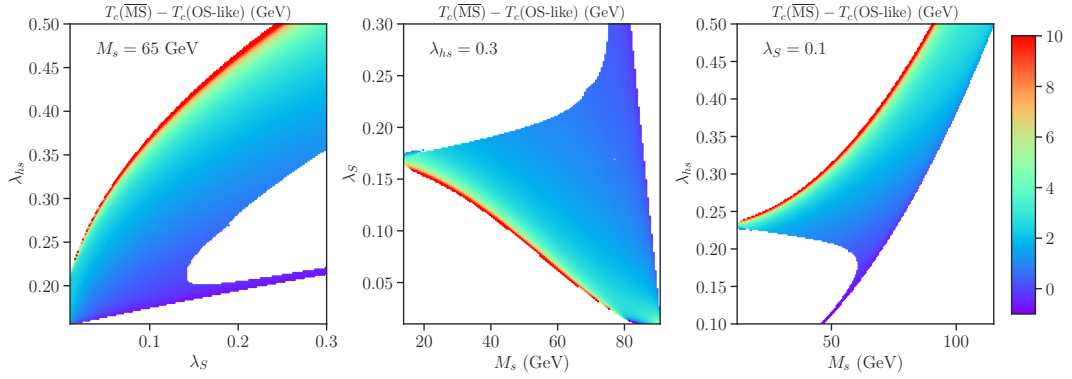


Figure 12: The difference in critical temperature T_c between the $\overline{\text{MS}}$ and OS-like schemes in 2-dimensional scans, under the same settings. In the blank regions there are no points with a FOPT in both the $\overline{\text{MS}}$ and OS-like schemes. We fix $m_s = 62.5$ GeV in the left panel, $\lambda_{hs} = 0.3$ in the middle panel, and $\lambda_s = 0.1$ in the right panel.

independent of renormalisation scheme, and the PRM method which depends on the $\overline{\text{MS}}$ scheme. In both the $\overline{\text{MS}}$ scheme and the OS-like scheme, we use $\xi = 0$, the Arnold-Espinosa method for daisy resummation, and resum the Goldstone boson mass to solve the GC. The renormalisation scale in the $\overline{\text{MS}}$ scheme is set to m_t . For the $\overline{\text{MS}}$ potential used in the PRM method we adopt the same settings as in the $\overline{\text{MS}}$ scheme, except that we do not resum daisies.

Since the zero-temperature one-loop corrections depend on the choice of renormalisation scheme, the tadpole conditions result in different Lagrangian parameters, λ_h , μ_h and μ_s , in each scheme. Therefore, every part of the effective potential can be different in the $\overline{\text{MS}}$ and the OS-like schemes. However, the differences in T_c and γ_{EW} are typically

mild with the OS and $\overline{\text{MS}}$ schemes giving surprisingly similar results for the choice of renormalisation scale we make for the $\overline{\text{MS}}$ scheme ($Q = m_t$). It was also found in previous work that the OS-like result lies within the scale variation uncertainty [64]. This suggests that the differences to the OS-like scheme is not really accessing any higher-order corrections beyond the $\overline{\text{MS}}$ scale variation though the very close agreement we see must be coincidental in nature.

Except for the flat region $\lambda_{hs} < 0.17$ in the left panels and $m_s > 88 \text{ GeV}$ in the right panels of Fig. 11, T_c in the $\overline{\text{MS}}$ scheme is larger than T_c in the OS-like scheme, and vice-versa for the transition strengths in the bottom panels. With critical temperature decreasing, the difference $\Delta T_c = T_c(\overline{\text{MS}}) - T_c(\text{OS-like})$ increases monotonically from about 1 GeV to more than 10 GeV. This occurs for the whole parameter space, which can be seen from the results of the two-dimensional scans in Fig. 12.

The T_c of the high-temperature approximation and the PRM method are far lower than that of the OS-like scheme and the $\overline{\text{MS}}$ scheme. There is no result for small λ_{hs} , large λ_s and m_s , because the expression of T_c of HT, eq. (25), assumes a minimum of the form $(0, v_s^{\text{high}})$ exists at T_c . The differences between results from the HT approximation and the OS-like scheme are easy to understand. They both use tree-level tadpole conditions to solve the Lagrangian parameters, λ_h , μ_h^2 and μ_s^2 , which results in exactly the same tree-level potential. The one-loop finite-temperature corrections are also supposed to be similar. Since the zero-temperature one-loop correction in the OS-like scheme is zero at the EW VEV, the only obvious difference is the zero-temperature one-loop correction of the OS-like scheme around the minimum of $\phi_h = 0$. In this minimum, the fermions and vectors are massless, and the only non-vanishing contribution to the zero-temperature one-loop correction comes from scalars and is always positive. Therefore, to compensate this increase in the potential, the OS-like scheme needs larger thermal corrections, i.e. higher temperature than in the HT approximation, to achieve degenerate minima. As for the PRM method, it also uses tree-level tadpole conditions, and the zero-temperature one-loop corrections in the $\overline{\text{MS}}$ scheme reduce the vacuum energy gap, so it leads to lower T_c than the HT approximation. However, in the HT approximation, both the vacua tend towards the origin as temperature increases, as can be seen in appendix A, which also reduces the vacuum energy gap, while the vacua in the PRM method are fixed. These two impacts cancel each other to some extent, leading to similar results in these two schemes. In contrast the results can also diverge more at higher critical temperatures. In that case the HT expansion is, as you would expect, becoming a better approximation of the $\overline{\text{MS}}$ calculation and gets closer to the $\overline{\text{MS}}$ result.

4.5 Comparison in whole parameter space

Here we compare all the possible changes investigated above in the whole parameter space. As shown in Fig. 13 on 2-dimensional planes, changing the renormalisation scale between $\frac{1}{2}m_t$ and $2m_t$ or changing the gauge parameter between $\xi = 0$ and 25 always induce the greatest changes in the properties of the FOPT. The impact of the treatment of daisies (Arnold-Espinosa versus Parwani), the GC, and the renormalisation scheme dependence ($\overline{\text{MS}}$ versus OS-like) are always subdominant.

In Fig. 14, we show the greatest uncertainty of each point, which was the renormalisation scale uncertainty or gauge uncertainty, in a 3-dimensional random scan. We sampled

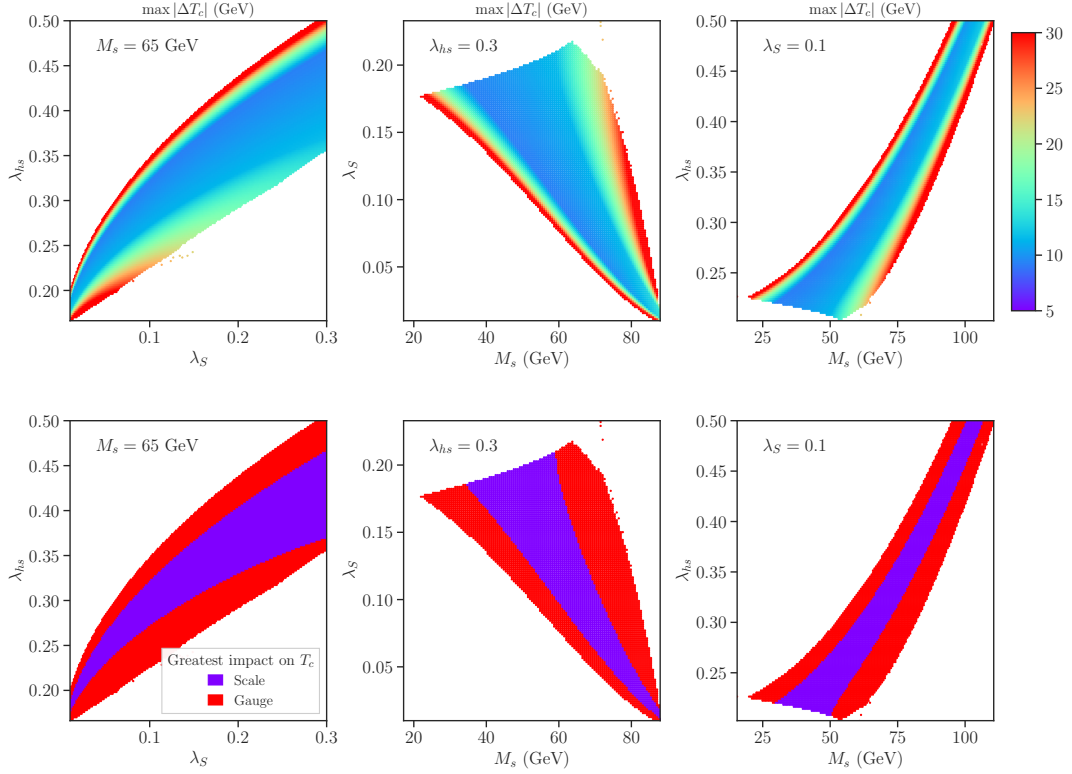


Figure 13: Maximum change in the critical temperature from changing the gauge, renormalisation scale, renormalisation scheme or treatment of daisies. We show the magnitude (upper panels) and source (lower panels) of the maximum change.

10^5 points with flat priors in the parameter space of

$$\lambda_{hs} \in [0.1, 0.5], \quad \lambda_s \in [0, 0.3], \quad m_s \in [10 \text{ GeV}, 110 \text{ GeV}]. \quad (40)$$

With these choices, about 20% of points had a FOPT at $\xi = 0$ and $Q = m_t$. Of those points, about 50% didn't have a FOPT at $\xi = 25$ and about 10% didn't have a FOPT at either $Q = \frac{1}{2}m_t$ or $2m_t$ (or both). In about 80% of cases gauge dependence was the greatest source of uncertainty. The top panels show the samples on planes of Lagrangian parameters with points with the smallest scale uncertainty shown on top. There are no strong trends on these planes, though samples of small uncertainty tend to lie at large m_s . In the bottom panels, the uncertainties are shown versus T_c and γ_{EW} , colored by the source of the maximal uncertainty. When $T_c < 100 \text{ GeV}$, varying the gauge parameter between 0 – 25 always results in a greater change in the critical temperature than varying the renormalisation scale between $\frac{1}{2}m_t - 2m_t$. When $T_c > 100 \text{ GeV}$, on the other hand, varying the renormalisation scale can have the greatest impact, and the lower bound of maximal uncertainty on T_c is given by points for which the maximum uncertainty comes from changing the renormalisation scale. The relative maximal uncertainty on T_c derived from gauge dependence decreases with T_c increasing, while for scale dependence the relative maximal uncertainty always lies around 10%. Conversely, varying the renormalisation scale can have the greatest impact on γ_{EW} for small γ_{EW} , and $\max |\Delta\gamma_{EW}|/\gamma_{EW}$ derived from gauge dependence increase with γ_{EW} increasing. The relative maximal un-

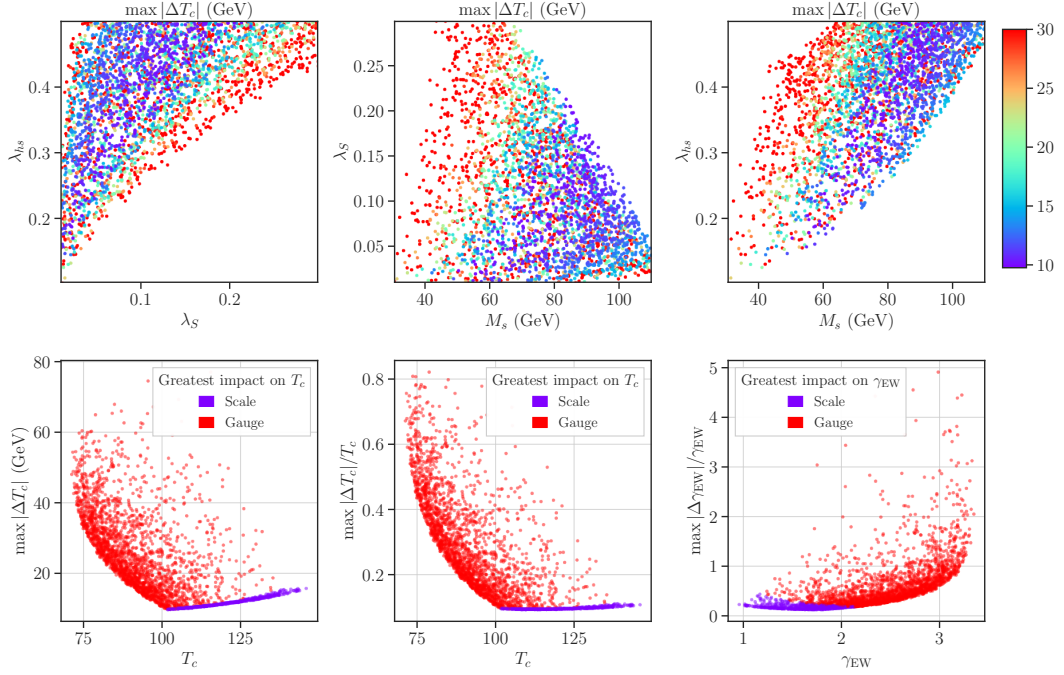


Figure 14: Results from three-dimensional scans. In the top panels, we show the maximum change in the critical temperature on two-dimensional planes, where points of small uncertainty are on top of points of large uncertainty. In the bottom panels, we show the relationship between the maximum changes in T_c and γ_{EW} and their values.

certainty on γ_{EW} can scarcely reach about 500%, because large γ_{EW} corresponds small T_c , which become sensitive to the Lagrangian parameters.

The relative uncertainties can be as large as 100% when one of the $T_c \simeq 0$ GeV, but it is rare to encounter such cases in general scans because the parameters need to be fine-tuned to achieve low T_c . In Fig. 15, we display the distribution of relative and absolute uncertainties of T_c and γ of the 3-dimensional random scan. We find that absolute (relative) uncertainties of T_c and γ for most of the samples are smaller than 13 GeV (10%) and 0.4 (14%), respectively, but that no samples have uncertainties smaller than 10 GeV (9%) and 0.19 (11%). In extreme and rare cases, $\max |\Delta T_c|$ and $\max |\Delta \gamma_{EW}|$ reached 77 GeV and 0.49 respectively, and in an even more detailed scan the maximum uncertainty would be even larger. We see from the colors of the bars that for points with moderate or large uncertainties, the greatest source of uncertainty is almost always gauge dependence. This final remark is subject to the choice of scales and gauge parameters that we compare. With a smaller range of gauge parameters, $\xi = 0$ to $\xi = 3$, it was instead found that scale dependence was the greatest source of uncertainty for the majority of the parameter space.

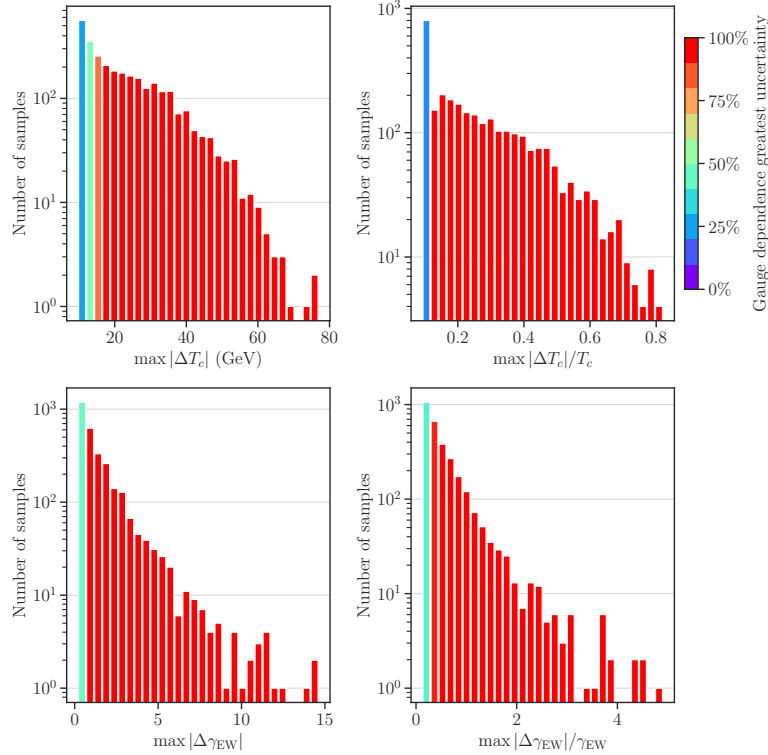


Figure 15: Distributions of maximum change in the critical temperature (upper) and transition strength (lower) for samples shown in Fig. 14. The bars are colored by the fraction of points for which gauge dependence was the greatest source of uncertainty.

5 Conclusions

First-order phase transitions could have occurred in the history of our Universe, helped lead to the abundance of matter over anti-matter, and left behind observable gravitational wave signatures. In perturbative calculations in models of particle physics, however, the properties and occurrence of first-order phase transitions are sensitive to somewhat arbitrary choices, including choices of renormalisation scale and gauge. We investigated the impact of those choices in detail, using the electroweak phase transition in the SM extended by a real scalar singlet as a benchmark. We explored the three-dimensional parameter space of this model through one- and two-dimensional slices as well as three-dimensional scans.

We refrain from making recommendations about the best choices, and instead wish to emphasise the sizes of the uncertainties and which choices influence the results the most. The scale dependence in the $\overline{\text{MS}}$ scheme and gauge dependence were the most significant sources of arbitrariness. Regarding the former, we found that

- Changing Q from $\frac{1}{2}m_t$ to $2m_t$ induced moderate changes in the PT properties, typically less than about 10%.
- Scale dependence was particularly severe in the PRM scheme, and only somewhat alleviated by using RGE running.

- Counter-intuitively, applying two-loop RGE running in the $\overline{\text{MS}}$ scheme worsened scale dependence, possibly because this was not a strict fixed-order calculation and because we neglected the anomalous dimension of the fields.
- Similarly, the Parwani method worsened scale dependence, despite the possibility of cancellations in the scale dependence between the CW and finite-temperature parts of the potential.
- Whenever the PT properties strongly depend on the choices of Lagrangian parameters, they inevitably strongly depend on the choice of scale.
- Only about 10% of our points with a FOPT at $Q = m_t$ didn't have a FOPT at both $Q = \frac{1}{2}m_t$ and $2m_t$.

In an OS-like scheme, on the other hand, we found quite similar results to the $\overline{\text{MS}}$ scheme at $Q = m_t$, though in extreme cases the differences in critical temperature reached about 10 GeV. Regarding gauge dependence, we found that

- In the $\overline{\text{MS}}$ scheme the gauge dependence of the critical temperature and transition strength could be $\mathcal{O}(100\%)$ in extreme cases when ξ was varied from 0 to 25 for both the R_ξ and covariant gauges, though was typically milder.
- When varying between $\xi = 0$ and 1, with an upper bound consistent with an $\mathcal{O}(1)$ bound from perturbativity [61, 76], the gauge dependence was extremely mild.
- The gauge-independent PRM and HT predictions for PT properties were similar to each other and quite different from those from the $\overline{\text{MS}}$ method.
- Despite being gauge independent, gauge dependence creeps into the PRM and HT methods when Lagrangian parameters are determined from tadpole conditions or mass constraints in a gauge-dependent way. In these cases the gauge dependence was similar to that in the $\overline{\text{MS}}$ scheme.
- In the R_ξ gauge, we can avoid the GC at $\xi = 0$ by using the Higgs mass squared parameter obtained from one-loop tadpole conditions in the calculation of the field-dependent Goldstone masses. However, even with this approach, Goldstone catastrophes still occurred for other choices of ξ for which Goldstones were massless in the EW vacuum.
- About 50% of our points with a FOPT at $\xi = 0$ didn't have a FOPT at $\xi = 25$.

Finally, the impact of the different treatments of daisy diagrams and the GC were relatively small, always changing the critical temperature by less than about 10 GeV.

In summary, we investigated the major sources of arbitrariness in perturbative treatments of FOPTs, including renormalisation scales and schemes, and gauges and gauge fixing parameters. We found that moderate variations in these choices, especially the choice of gauge parameter, may lead to significant changes in the predictions for the FOPTs.

Acknowledgements

The work of P.A. in this paper has been supported by the Australian Research Council Future Fellowship grant FT160100274 and the National Natural Science Foundation of China (NNSFC) Research Fund for International Excellent Young Scientists, grant No. 12150610460. The work of P.A. and C.B. was also supported by the Australian Research Council Discovery Project grants DP180102209 and DP210101636. The work of L.M. was supported by an Australian Government Research Training Program (RTP) Scholarship and a Monash Graduate Excellence Scholarship (MGES). The work of Y.Z. was supported by the NNSFC under grant No. 12105248, by CAS Peng Huanwu Junior Visiting Professor Program and by Zhengzhou University Young Talent Program. This project was also undertaken with the assistance of resources and services from the National Computational Infrastructure, which is supported by the Australian Government. We thank Astronomy Australia Limited for financial support of computing resources, and the Astronomy Supercomputer Time Allocation Committee for its generous grant of computing time. The work of GW is supported by World Premier International Research Center Initiative (WPI), MEXT, Japan.

A Phase structure

In the SSM, the FOPT almost always happens between a minimum of the form $\phi_s \equiv (v_h^{\text{high}} = 0, v_s^{\text{high}})$ and minimum of the form $\phi_h \equiv (v_h^{\text{low}}, v_s^{\text{low}} = 0)$, as shown in the top left panel in Fig. 16. Fig. 16 shows the evolution of minima of the effective potential with temperature for different cases. In all the cases, there is only one minimum at high temperature, $T > 400$ GeV. In the top left panel, a second-order phase transition occurs at $T \simeq 300$ GeV from the origin to a minimum at $(\phi_h = 0, \phi_s \neq 0)$, indicated by orange lines. With temperature decreasing, a FOPT becomes possible below $T_c = 114$ GeV, after which the minimum at $(\phi_h \neq 0, \phi_s = 0)$ becomes the deepest minimum of the effective potential.

There are parameter points for which no FOPT occurs during the evolution of the potential with temperature. They may be split into three cases:

- The minimum at $(\phi_h \neq 0, \phi_s = 0)$ is never the deepest minimum, so there is no transition from the minimum at $(\phi_h = 0, \phi_s \neq 0)$ to it, as shown in the top right panel of Fig. 16. This happens for large λ_{hs} , small λ_s and m_S , i.e. the top left corners of the λ_s - λ_{hs} and m_s - λ_{hs} planes in Fig. 4.
- There is never a minimum at $(\phi_h = 0, \phi_s \neq 0)$ during the evolution, and the phase transition from the origin to $(\phi_h \neq 0, \phi_s = 0)$ is not a strong first-order transition. This is similar to the situation in the SM. This case is displayed in the bottom left panel of Fig. 16, and corresponds to small λ_{hs} and large λ_s and M_S . This kind of transition is ignored in 2-dimensional and 3-dimensional scans.
- The phase transition from the minimum at $(\phi_h = 0, \phi_s \neq 0)$ to the minimum at $(\phi_h \neq 0, \phi_s = 0)$ is not first-order, which is presented in the bottom right panel of Fig. 16. It is caused by large λ_s and small m_s .

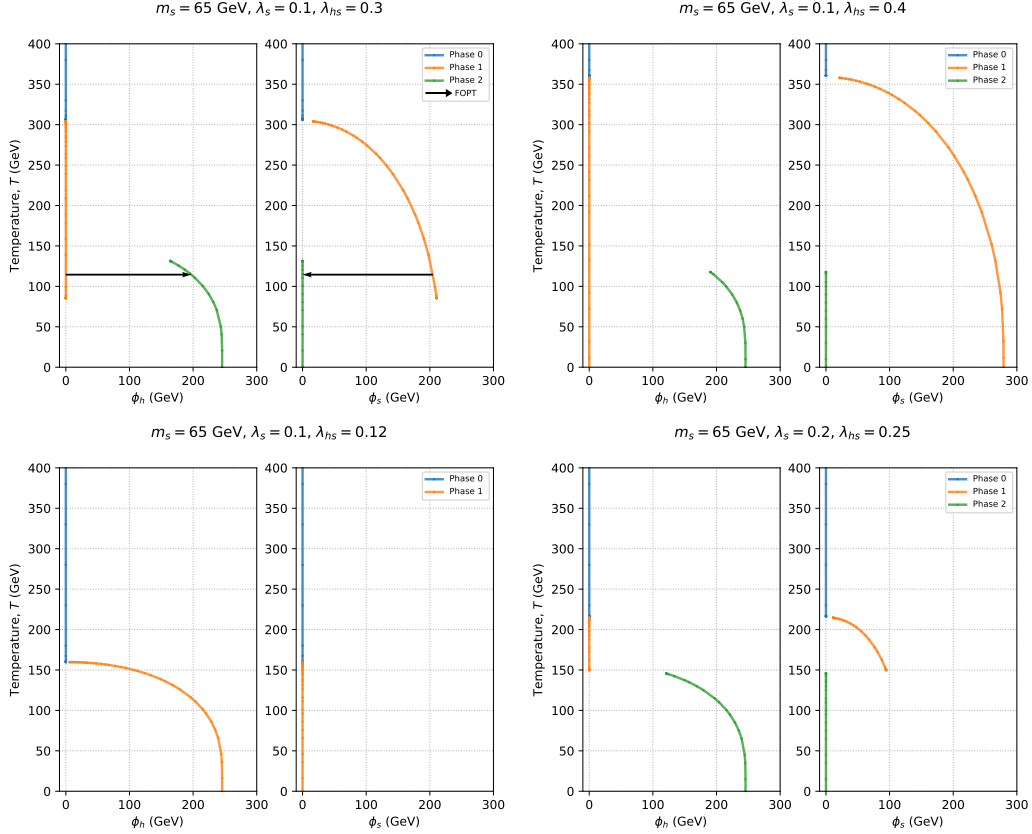


Figure 16: Typical phase structures in the SSM. The lines show the field values at a particular minimum as a function of temperature. The arrows indicate that at that temperature the two phases linked by the arrows are degenerate and thus that a FOPT could occur in the direction of the arrow.

In our calculations, there are more complicated phase structures than above cases, caused by numerical problems, such as the fact that the thermal functions are not smooth. To maintain consistency, unless otherwise stated we only compare and show the type of FOPT shown in the top left panel of Fig. 16 in our results.

B Benchmark point

In Tab. 2, we present input parameters, parameters extracted from tadpole conditions, critical temperature and transition strength of the benchmark point used in Sec. 4, for different gauge parameters. Here we used the $\overline{\text{MS}}$ scheme in R_ξ gauges, the Arnold-Espinosa technique to resum daisy terms, `GC_SelfEnergy_Sol` to solve the GC and set $Q = m_t$.

| m_s | λ_s | λ_{hs} | ξ | μ_h^2 | μ_s^2 | λ_h | T_c | γ_{EW} | $v_s^{\text{high}}(T_c)$ | $v_h^{\text{low}}(T_c)$ |
|-------|-------------|----------------|-------|-----------|-----------|-------------|--------|---------------|--------------------------|-------------------------|
| 65 | 0.1 | 0.3 | 0 | -8720.10 | -4860.43 | 0.129 | 113.54 | 1.79 | 211.04 | 203.53 |
| | | | 25 | -7721.33 | -5267.03 | 0.106 | 114.56 | -1.90 | 220.43 | -217.13 |
| | | | | -998.8 | 406.6 | 0.023 | -1.016 | 3.69 | -9.39 | -13.60 |
| 58 | 0.1 | 0.3 | 0 | -8723.64 | -5722.60 | 0.129 | 94.90 | 2.36 | 234.75 | 223.58 |
| | | | 25 | -7725.12 | -6128.86 | 0.106 | 82.86 | 2.87 | 245.66 | 237.40 |
| | | | | -998.53 | 406.26 | 0.023 | 12.04 | -0.51 | -10.91 | -13.82 |
| 72 | | | 0 | -8716.74 | -3900.27 | 0.129 | 129.87 | 1.36 | 180.70 | 176.87 |
| | | | 25 | -7717.74 | -4307.17 | 0.106 | 142.13 | -1.31 | 185.05 | -186.62 |
| | | | | -999.00 | 406.90 | 0.023 | -12.26 | 2.68 | -4.36 | -9.75 |
| 65 | 0.09 | 0.3 | 0 | -8720.11 | -4862.84 | 0.129 | 108.47 | 1.94 | 224.43 | 209.92 |
| | | | 25 | -7721.34 | -5269.44 | 0.106 | 105.38 | 2.13 | 235.65 | 224.44 |
| | | | | -998.77 | 406.60 | 0.023 | 3.09 | -0.19 | -11.23 | -14.52 |
| | 0.11 | | 0 | -8720.09 | -4858.02 | 0.129 | 117.62 | 1.68 | 199.57 | 197.81 |
| | | | 25 | -7721.32 | -5264.62 | 0.106 | 121.80 | 1.73 | 207.02 | 210.41 |
| | | | | -998.77 | 406.59 | 0.023 | -4.19 | -0.05 | -7.45 | -12.61 |
| 65 | 0.1 | 0.27 | 0 | -8718.11 | -3953.10 | 0.129 | 128.62 | 1.40 | 183.27 | 179.53 |
| | | | 25 | -7719.28 | -4319.66 | 0.106 | 140.41 | 1.35 | 185.10 | 189.13 |
| | | | | -998.83 | 366.56 | 0.023 | -11.79 | 0.05 | -1.82 | -9.60 |
| | | 0.33 | 0 | -8722.40 | -5766.98 | 0.129 | 94.00 | -2.39 | 236.00 | 224.32 |
| | | | 25 | -7723.71 | -6213.46 | 0.106 | 78.95 | -3.03 | 248.13 | -239.03 |
| | | | | -998.69 | 446.47 | 0.023 | 15.05 | 0.64 | -12.13 | 14.71 |

Table 2: Values of Lagrangian parameters, critical temperature, γ_{EW} , and VEVs for points around the benchmark point in the $\overline{\text{MS}} + \text{GC_SelfEnergy_Sol}$ scheme. All dimensionful quantities are in GeV or GeV^2 . The blue numbers show difference between quantities evaluated at $\xi = 0$ and 25.

C Mass spectrum

The field-dependent Higgs and singlet masses are given by the eigenvalues of the scalar mass matrix

$$M_\phi^2(\phi) = \begin{pmatrix} \frac{\partial^2 V}{\partial \phi_h^2} & \frac{\partial^2 V}{\partial \phi_h \partial \phi_s} \\ \frac{\partial^2 V}{\partial \phi_h \partial \phi_s} & \frac{\partial^2 V}{\partial \phi_s^2} \end{pmatrix}. \quad (41)$$

When evaluated at the EW VEV, they are the masses of the Higgs and singlet. The off-diagonal terms vanish in the \mathbb{Z}_2 -symmetric model because $v_s = 0$ at $T = 0$, such that the masses are simply the diagonal entries, which are given in eqs. (10) and (11). The Z boson and photon field-dependent masses are similarly obtained as eigenvalues of the neutral gauge boson mass matrix

$$M_{A^0}^2(\phi) = \begin{pmatrix} \frac{1}{4}g^2\phi_h^2 & -\frac{1}{4}gg'\phi_h^2 \\ -\frac{1}{4}gg'\phi_h^2 & \frac{1}{4}g'^2\phi_h^2 \end{pmatrix}. \quad (42)$$

We use the third family approximation for the fermions, and so include the masses

$$m_{b,t,\tau}^2(\phi) = \frac{y_{b,t,\tau}^2}{2} \phi_h^2. \quad (43)$$

This ignores fermions lighter than the bottom quark.

The scalars and longitudinal components of the gauge bosons receive Debye corrections at finite temperature. The Debye corrections are diagonal matrices that are added to the corresponding mass matrices before diagonalisation, with eq. (41) becoming

$$M_\phi^2(\phi, T) = \begin{pmatrix} \frac{\partial^2 V}{\partial \phi_h^2} + c_h T^2 & \frac{\partial^2 V}{\partial \phi_h \partial \phi_s} \\ \frac{\partial^2 V}{\partial \phi_h \partial \phi_s} & \frac{\partial^2 V}{\partial \phi_s^2} + c_s T^2 \end{pmatrix}, \quad (44)$$

where the scalar Debye coefficients are

$$c_h = \frac{1}{48} \left[9g^2 + 3g'^2 + 2 \left(6y_t^2 + 6y_b^2 + 2y_\tau^2 + 12\lambda_h + \lambda_{hs} \right) \right], \quad (45)$$

$$c_s = \frac{1}{12} [2\lambda_{hs} + 3\lambda_s]. \quad (46)$$

For the longitudinal components of the gauge bosons, eq. (42) becomes

$$M_{A_L^0}^2(\phi) = \begin{pmatrix} \frac{1}{4}g^2\phi_h^2 + \frac{11}{6}g^2T^2 & -\frac{1}{4}gg'\phi_h^2 \\ -\frac{1}{4}gg'\phi_h^2 & \frac{1}{4}g'^2\phi_h^2 + \frac{11}{6}g'^2T^2 \end{pmatrix}. \quad (47)$$

Lastly, the Goldstone boson masses receive the Debye correction $c_h T^2$ in both the R_ξ and covariant gauges, and the longitudinal component of the W boson receives the Debye correction $\frac{11}{6}g^2 T^2$. Performing the diagonalisation leaves the following field-dependent

thermal boson masses,

$$\begin{aligned}\overline{m}_h^2(\phi, T) = & -(\mu_h^2 + \mu_s^2) + 3(\lambda_h \phi_h^2 + \lambda_s \phi_s^2) + \frac{1}{2}\lambda_{hs}(\phi_h^2 + \phi_s^2) + (c_h + c_s)T^2 \\ & + \left[\left(-(\mu_h^2 - \mu_s^2) + 3(\lambda_h \phi_h^2 - \lambda_s \phi_s^2) - \frac{1}{2}\lambda_{hs}(\phi_h^2 - \phi_s^2) + (c_h - c_s)T^2 \right)^2 \right. \\ & \left. + 4\lambda_{hs}^2 \phi_h^2 \phi_s^2 \right]^{\frac{1}{2}},\end{aligned}\tag{48}$$

$$\begin{aligned}\overline{m}_s^2(\phi, T) = & -(\mu_h^2 + \mu_s^2) + 3(\lambda_h \phi_h^2 + \lambda_s \phi_s^2) + \frac{1}{2}\lambda_{hs}(\phi_h^2 + \phi_s^2) + (c_h + c_s)T^2 \\ & - \left[\left(-(\mu_h^2 - \mu_s^2) + 3(\lambda_h \phi_h^2 - \lambda_s \phi_s^2) - \frac{1}{2}\lambda_{hs}(\phi_h^2 - \phi_s^2) + (c_h - c_s)T^2 \right)^2 \right. \\ & \left. + 4\lambda_{hs}^2 \phi_h^2 \phi_s^2 \right]^{\frac{1}{2}},\end{aligned}\tag{49}$$

$$m_G^2(\phi, T) = \mu_h^2 + \lambda_h \phi_h^2 + \frac{1}{2}\lambda_{hs}\phi_s^2 + c_h T^2,\tag{50}$$

$$m_{W_T}^2(\phi) = \frac{g^2}{4}\phi_h^2,\tag{51}$$

$$m_{W_L}^2(\phi, T) = \frac{g^2}{4}\phi_h^2 + \frac{11}{6}g^2 T^2,\tag{52}$$

$$m_{\gamma_T}^2(\phi) = 0,\tag{53}$$

$$\begin{aligned}m_{\gamma_L}^2(\phi, T) = & \frac{1}{24} \left[(g^2 + g'^2) (3\phi_h^2 + 22T^2) \right. \\ & \left. - \sqrt{9(g^2 + g'^2)^2 \phi_h^4 + 44T^2 (g^2 - g'^2)^2 (3\phi_h^2 + 11T^2)} \right],\end{aligned}\tag{54}$$

$$m_{Z_T}^2(\phi) = \frac{g^2 + g'^2}{4}\phi_h^2,\tag{55}$$

$$\begin{aligned}m_{Z_L}^2(\phi, T) = & \frac{1}{24} \left[(g^2 + g'^2) (3\phi_h^2 + 22T^2) \right. \\ & \left. + \sqrt{9(g^2 + g'^2)^2 \phi_h^4 + 44T^2 (g^2 - g'^2)^2 (3\phi_h^2 + 11T^2)} \right].\end{aligned}\tag{56}$$

At zero temperature, the photon mass vanishes as expected. The degrees of freedom for these masses are $n_h = n_s = 1$, $n_G = 3$, $n_{\gamma_L} = n_{Z_L} = 2$, $n_{\gamma_T} = n_{Z_T} = 1$, $n_{W_L} = 4$, $n_{W_T} = 2$, $n_\tau = 4$, and $n_b = n_t = 12$. The degrees of freedom for the scalar particles differs in the covariant gauge, as discussed in Sec. 2.2.

D Numerical uncertainties

All the numerical results presented above are obtained using **PhaseTracer** [60]. In the manual [60], we have shown the numerical uncertainty in the calculation of a phase transition using the HT method and the SSM as an example. The differences between the

analytic formulae and the numerical results from **PhaseTracer** are less than about 0.01%. In this section, we further discuss numerical uncertainties and issues we encountered in this work.

The SM parameters involved in the effective potential models include mass of the SM-like Higgs m_h , SM EW VEV at zero-temperature v , the gauge coupling constants g and g' , and the Yukawa coupling y_t , y_b and y_τ . Since we use **FlexibleSUSY** for our RGE running, we use the default values in **FlexibleSUSY** in all the models to be consistent,

$$\begin{aligned} m_h &= 125.25 \text{ GeV}, \quad v = 247.4554 \text{ GeV}, \quad g = 0.6477, \quad g' = 0.3586, \\ y_t &= 0.9341, \quad y_b = 0.01547, \quad y_\tau = 0.010014. \end{aligned} \tag{57}$$

Modifying these values will of course affect the values of T_c and γ_{EW} . However, by regenerating all the results with $m_h = 126.0 \text{ GeV}$ and $v = 246 \text{ GeV}$ we have checked that it will not qualitatively change our above discussions and conclusions.

There is no closed-form solution for calculation of the thermal functions, $J_B(y^2)$ and $J_F(y^2)$ in eq. (23). The precision of several numerical methods to do this have been fully discussed in [105]. **PhaseTracer** adopt the same method as **CosmoTransitions** [106], calculating a series of points by quadrature integration in **SciPy** library for **Python** and then using B-spline interpolation to get thermal functions of any point. This method is very fast and pretty accurate except around $y^2 = 0$. We find that the second-order derivative of the thermal function obtained in this way is not continuous at $y^2 = 0$. Fortunately, it is very rare that the minima at T_c encounter $y^2 = 0$, so the T_c of FOPT is not ruined.

Nevertheless, the discontinuity of the second-order derivatives of the thermal function around zero mass may introduce an additional artificial minimum in the effective potential, which will form an artificial phase. In some cases, there is a transition between this artificial phase and an ordinary phase, especially if the Arnold-Espinosa method is used for daisy resummation. The Parwani method can partially avoid this situation, because the Debye corrections to the field-dependent masses are positive such that we do not encounter zero masses at the minimum. In any case, the artificial phase cannot affect our results because we focus on the FOPT described in appendix A, and ignore other transitions.

As already discussed, the number density of parameter points sampled in the scan will impact the maximum change in the critical temperature and transition strength found. Since the maximum change occurs when T_c is very sensitive to the input parameters, the more detailed scan we have, the larger the maximum uncertainty we are likely to obtain. Besides, the local minimum finding algorithm adopted in **PhaseTracer** has large numerical uncertainty when the potential around the minimum tends to be flat, and has a chance of misidentifying a saddle point as a minimum. This causes noise in our plots. The more detailed scan we have, the more noisy points will appear.

These numerical problems do not only exist in the SSM or only when using **PhaseTracer**. As the SSM is quite a simple model, we anticipate that further issues and larger uncertainties could be found in more complicated models. Therefore, they should be carefully considered in any perturbative calculations of phase transitions.

References

- [1] C. Caprini et al., *Detecting gravitational waves from cosmological phase transitions with LISA: an update*, *JCAP* **03** (2020) 024, [[1910.13125](#)].
- [2] M. J. Ramsey-Musolf, *The electroweak phase transition: a collider target*, *JHEP* **09** (2020) 179, [[1912.07189](#)].
- [3] J. L. Barrow et al., *Theories and Experiments for Testable Baryogenesis Mechanisms: A Snowmass White Paper*, [2203.07059](#).
- [4] A. D. Sakharov, *Violation of CP Invariance, C asymmetry, and baryon asymmetry of the universe*, *Pisma Zh. Eksp. Teor. Fiz.* **5** (1967) 32–35.
- [5] K. Kajantie, M. Laine, K. Rummukainen and M. E. Shaposhnikov, *The Electroweak phase transition: A Nonperturbative analysis*, *Nucl. Phys. B* **466** (1996) 189–258, [[hep-lat/9510020](#)].
- [6] K. Kajantie, M. Laine, K. Rummukainen and M. E. Shaposhnikov, *Is there a hot electroweak phase transition at $m_H \gtrsim m_W$?*, *Phys. Rev. Lett.* **77** (1996) 2887–2890, [[hep-ph/9605288](#)].
- [7] K. Kajantie, M. Laine, K. Rummukainen and M. E. Shaposhnikov, *A Nonperturbative analysis of the finite- T phase transition in $SU(2) \times U(1)$ electroweak theory*, *Nucl. Phys. B* **493** (1997) 413–438, [[hep-lat/9612006](#)].
- [8] F. Csikor, Z. Fodor and J. Heitger, *Endpoint of the hot electroweak phase transition*, *Phys. Rev. Lett.* **82** (1999) 21–24, [[hep-ph/9809291](#)].
- [9] M. D’Onofrio and K. Rummukainen, *Standard model cross-over on the lattice*, *Phys. Rev. D* **93** (2016) 025003, [[1508.07161](#)].
- [10] M. Pietroni, *The Electroweak phase transition in a nonminimal supersymmetric model*, *Nucl. Phys. B* **402** (1993) 27–45, [[hep-ph/9207227](#)].
- [11] J. M. Cline and P.-A. Lemieux, *Electroweak phase transition in two Higgs doublet models*, *Phys. Rev. D* **55** (1997) 3873–3881, [[hep-ph/9609240](#)].
- [12] S. W. Ham, S. K. OH, C. M. Kim, E. J. Yoo and D. Son, *Electroweak phase transition in a nonminimal supersymmetric model*, *Phys. Rev. D* **70** (2004) 075001, [[hep-ph/0406062](#)].
- [13] K. Funakubo, S. Tao and F. Toyoda, *Phase transitions in the NMSSM*, *Prog. Theor. Phys.* **114** (2005) 369–389, [[hep-ph/0501052](#)].
- [14] V. Barger, P. Langacker, M. McCaskey, M. Ramsey-Musolf and G. Shaughnessy, *Complex Singlet Extension of the Standard Model*, *Phys. Rev. D* **79** (2009) 015018, [[0811.0393](#)].
- [15] D. J. H. Chung and A. J. Long, *Electroweak Phase Transition in the $\mu\nu$ SSM*, *Phys. Rev. D* **81** (2010) 123531, [[1004.0942](#)].

- [16] J. R. Espinosa, T. Konstandin and F. Riva, *Strong Electroweak Phase Transitions in the Standard Model with a Singlet*, *Nucl. Phys. B* **854** (2012) 592–630, [[1107.5441](#)].
- [17] T. A. Chowdhury, M. Nemevsek, G. Senjanovic and Y. Zhang, *Dark Matter as the Trigger of Strong Electroweak Phase Transition*, *JCAP* **02** (2012) 029, [[1110.5334](#)].
- [18] G. Gil, P. Chankowski and M. Krawczyk, *Inert Dark Matter and Strong Electroweak Phase Transition*, *Phys. Lett. B* **717** (2012) 396–402, [[1207.0084](#)].
- [19] M. Carena, G. Nardini, M. Quiros and C. E. Wagner, *MSSM Electroweak Baryogenesis and LHC Data*, *JHEP* **02** (2013) 001, [[1207.6330](#)].
- [20] J. M. No and M. Ramsey-Musolf, *Probing the Higgs Portal at the LHC Through Resonant di-Higgs Production*, *Phys. Rev. D* **89** (2014) 095031, [[1310.6035](#)].
- [21] G. C. Dorsch, S. J. Huber and J. M. No, *A strong electroweak phase transition in the 2HDM after LHC8*, *JHEP* **10** (2013) 029, [[1305.6610](#)].
- [22] D. Curtin, P. Meade and C.-T. Yu, *Testing Electroweak Baryogenesis with Future Colliders*, *JHEP* **11** (2014) 127, [[1409.0005](#)].
- [23] W. Huang, Z. Kang, J. Shu, P. Wu and J. M. Yang, *New insights in the electroweak phase transition in the NMSSM*, *Phys. Rev. D* **91** (2015) 025006, [[1405.1152](#)].
- [24] S. Profumo, M. J. Ramsey-Musolf, C. L. Wainwright and P. Winslow, *Singlet-catalyzed electroweak phase transitions and precision Higgs boson studies*, *Phys. Rev. D* **91** (2015) 035018, [[1407.5342](#)].
- [25] J. Kozaczuk, S. Profumo, L. S. Haskins and C. L. Wainwright, *Cosmological Phase Transitions and their Properties in the NMSSM*, *JHEP* **01** (2015) 144, [[1407.4134](#)].
- [26] M. Jiang, L. Bian, W. Huang and J. Shu, *Impact of a complex singlet: Electroweak baryogenesis and dark matter*, *Phys. Rev. D* **93** (2016) 065032, [[1502.07574](#)].
- [27] D. Curtin, P. Meade and H. Ramani, *Thermal Resummation and Phase Transitions*, *Eur. Phys. J. C* **78** (2018) 787, [[1612.00466](#)].
- [28] V. Vaskonen, *Electroweak baryogenesis and gravitational waves from a real scalar singlet*, *Phys. Rev. D* **95** (2017) 123515, [[1611.02073](#)].
- [29] G. Dorsch, S. Huber, T. Konstandin and J. No, *A Second Higgs Doublet in the Early Universe: Baryogenesis and Gravitational Waves*, *JCAP* **05** (2017) 052, [[1611.05874](#)].
- [30] P. Huang, A. J. Long and L.-T. Wang, *Probing the Electroweak Phase Transition with Higgs Factories and Gravitational Waves*, *Phys. Rev. D* **94** (2016) 075008, [[1608.06619](#)].

- [31] M. Chala, G. Nardini and I. Sobolev, *Unified explanation for dark matter and electroweak baryogenesis with direct detection and gravitational wave signatures*, *Phys. Rev. D* **94** (2016) 055006, [[1605.08663](#)].
- [32] P. Basler, M. Krause, M. Muhlleitner, J. Wittbrodt and A. Wlotzka, *Strong First Order Electroweak Phase Transition in the CP-Conserving 2HDM Revisited*, *JHEP* **02** (2017) 121, [[1612.04086](#)].
- [33] A. Beniwal, M. Lewicki, J. D. Wells, M. White and A. G. Williams, *Gravitational wave, collider and dark matter signals from a scalar singlet electroweak baryogenesis*, *JHEP* **08** (2017) 108, [[1702.06124](#)].
- [34] J. Bernon, L. Bian and Y. Jiang, *A new insight into the phase transition in the early Universe with two Higgs doublets*, *JHEP* **05** (2018) 151, [[1712.08430](#)].
- [35] G. Kurup and M. Perelstein, *Dynamics of Electroweak Phase Transition In Singlet-Scalar Extension of the Standard Model*, *Phys. Rev. D* **96** (2017) 015036, [[1704.03381](#)].
- [36] J. O. Andersen, T. Gorda, A. Helset, L. Niemi, T. V. I. Tenkanen, A. Tranberg et al., *Nonperturbative Analysis of the Electroweak Phase Transition in the Two Higgs Doublet Model*, *Phys. Rev. Lett.* **121** (2018) 191802, [[1711.09849](#)].
- [37] C.-W. Chiang, M. J. Ramsey-Musolf and E. Senaha, *Standard Model with a Complex Scalar Singlet: Cosmological Implications and Theoretical Considerations*, *Phys. Rev. D* **97** (2018) 015005, [[1707.09960](#)].
- [38] G. C. Dorsch, S. J. Huber, K. Mimasu and J. M. No, *The Higgs Vacuum Uplifted: Revisiting the Electroweak Phase Transition with a Second Higgs Doublet*, *JHEP* **12** (2017) 086, [[1705.09186](#)].
- [39] A. Beniwal, M. Lewicki, M. White and A. G. Williams, *Gravitational waves and electroweak baryogenesis in a global study of the extended scalar singlet model*, *JHEP* **02** (2019) 183, [[1810.02380](#)].
- [40] S. Bruggisser, B. Von Harling, O. Matsedonskyi and G. Servant, *Electroweak Phase Transition and Baryogenesis in Composite Higgs Models*, *JHEP* **12** (2018) 099, [[1804.07314](#)].
- [41] P. Athron, C. Balazs, A. Fowlie, G. Pozzo, G. White and Y. Zhang, *Strong first-order phase transitions in the NMSSM — a comprehensive survey*, *JHEP* **11** (2019) 151, [[1908.11847](#)].
- [42] K. Kainulainen, V. Keus, L. Niemi, K. Rummukainen, T. V. I. Tenkanen and V. Vaskonen, *On the validity of perturbative studies of the electroweak phase transition in the Two Higgs Doublet model*, *JHEP* **06** (2019) 075, [[1904.01329](#)].
- [43] L. Bian, Y. Wu and K.-P. Xie, *Electroweak phase transition with composite Higgs models: calculability, gravitational waves and collider searches*, *JHEP* **12** (2019) 028, [[1909.02014](#)].

- [44] H.-L. Li, M. Ramsey-Musolf and S. Willocq, *Probing a scalar singlet-catalyzed electroweak phase transition with resonant di-Higgs boson production in the 4b channel*, *Phys. Rev. D* **100** (2019) 075035, [[1906.05289](#)].
- [45] C.-W. Chiang and B.-Q. Lu, *First-order electroweak phase transition in a complex singlet model with \mathbb{Z}_3 symmetry*, *JHEP* **07** (2020) 082, [[1912.12634](#)].
- [46] K.-P. Xie, L. Bian and Y. Wu, *Electroweak baryogenesis and gravitational waves in a composite Higgs model with high dimensional fermion representations*, *JHEP* **12** (2020) 047, [[2005.13552](#)].
- [47] N. F. Bell, M. J. Dolan, L. S. Friedrich, M. J. Ramsey-Musolf and R. R. Volkas, *Two-Step Electroweak Symmetry-Breaking: Theory Meets Experiment*, *JHEP* **05** (2020) 050, [[2001.05335](#)].
- [48] A. Papaefstathiou and G. White, *The electro-weak phase transition at colliders: confronting theoretical uncertainties and complementary channels*, *JHEP* **05** (2021) 099, [[2010.00597](#)].
- [49] A. V. Kotwal, M. J. Ramsey-Musolf, J. M. No and P. Winslow, *Singlet-catalyzed electroweak phase transitions in the 100 TeV frontier*, *Phys. Rev. D* **94** (2016) 035022, [[1605.06123](#)].
- [50] H. H. Patel and M. J. Ramsey-Musolf, *Baryon Washout, Electroweak Phase Transition, and Perturbation Theory*, *JHEP* **07** (2011) 029, [[1101.4665](#)].
- [51] S. P. Martin, *Two Loop Effective Potential for a General Renormalizable Theory and Softly Broken Supersymmetry*, *Phys. Rev. D* **65** (2002) 116003, [[hep-ph/0111209](#)].
- [52] D. G. C. McKeon, *Renormalization Scheme Dependence with Renormalization Group Summation*, *Phys. Rev. D* **92** (2015) 045031, [[1503.03823](#)].
- [53] S. R. Coleman and E. J. Weinberg, *Radiative Corrections as the Origin of Spontaneous Symmetry Breaking*, *Phys. Rev. D* **7** (1973) 1888–1910.
- [54] P. B. Arnold, *Phase transition temperatures at next-to-leading order*, *Phys. Rev. D* **46** (1992) 2628–2635, [[hep-ph/9204228](#)].
- [55] O. Gould, S. Güyer and K. Rummukainen, *First-order electroweak phase transitions: a nonperturbative update*, [2205.07238](#).
- [56] P. Schicho, T. V. I. Tenkanen and G. White, *Combining thermal resummation and gauge invariance for electroweak phase transition*, [2203.04284](#).
- [57] A. Ekstedt, *Convergence of the nucleation rate for first-order phase transitions*, [2205.05145](#).
- [58] A. Ekstedt, O. Gould and J. Löfgren, *Radiative first-order phase transitions to next-to-next-to-leading-order*, [2205.07241](#).

- [59] A. Ekstedt, P. Schicho and T. V. I. Tenkanen, *DRalgo: a package for effective field theory approach for thermal phase transitions*, [2205.08815](#).
- [60] P. Athron, C. Balázs, A. Fowlie and Y. Zhang, *PhaseTracer: tracing cosmological phases and calculating transition properties*, *Eur. Phys. J. C* **80** (2020) 567, [[2003.02859](#)].
- [61] M. Garny and T. Konstandin, *On the gauge dependence of vacuum transitions at finite temperature*, *JHEP* **07** (2012) 189, [[1205.3392](#)].
- [62] C.-W. Chiang and E. Senaha, *On gauge dependence of gravitational waves from a first-order phase transition in classical scale-invariant $U(1)'$ models*, *Phys. Lett. B* **774** (2017) 489–493, [[1707.06765](#)].
- [63] S. Arunasalam and M. J. Ramsey-Musolf, *Tunneling Potentials for the Tunneling Action: Gauge Invariance*, [2105.07588](#).
- [64] C.-W. Chiang, Y.-T. Li and E. Senaha, *Revisiting electroweak phase transition in the standard model with a real singlet scalar*, *Phys. Lett. B* **789** (2019) 154–159, [[1808.01098](#)].
- [65] D. Croon, O. Gould, P. Schicho, T. V. I. Tenkanen and G. White, *Theoretical uncertainties for cosmological first-order phase transitions*, *JHEP* **04** (2021) 055, [[2009.10080](#)].
- [66] O. Gould and T. V. I. Tenkanen, *On the perturbative expansion at high temperature and implications for cosmological phase transitions*, *JHEP* **06** (2021) 069, [[2104.04399](#)].
- [67] A. Linde, *Infrared problem in the thermodynamics of the Yang-Mills gas*, *Physics Letters B* **96** (1980) 289–292.
- [68] A. Ekstedt, *Higher-order corrections to the bubble-nucleation rate at finite temperature*, *Eur. Phys. J. C* **82** (2022) 173, [[2104.11804](#)].
- [69] J. Elias-Miro, J. R. Espinosa and T. Konstandin, *Taming Infrared Divergences in the Effective Potential*, *JHEP* **08** (2014) 034, [[1406.2652](#)].
- [70] S. P. Martin, *Taming the Goldstone contributions to the effective potential*, *Phys. Rev. D* **90** (2014) 016013, [[1406.2355](#)].
- [71] J. R. Espinosa and T. Konstandin, *Resummation of Goldstone Infrared Divergences: A Proof to All Orders*, *Phys. Rev. D* **97** (2018) 056020, [[1712.08068](#)].
- [72] P. Ghorbani, *Vacuum structure and electroweak phase transition in singlet scalar dark matter*, *Phys. Dark Univ.* **33** (2021) 100861, [[2010.15708](#)].
- [73] PARTICLE DATA GROUP collaboration, P. A. Zyla et al., *Review of Particle Physics*, *PTEP* **2020** (2020) 083C01.

- [74] K. Fujikawa, B. W. Lee and A. I. Sanda, *Generalized Renormalizable Gauge Formulation of Spontaneously Broken Gauge Theories*, *Phys. Rev. D* **6** (1972) 2923–2943.
- [75] S. P. Martin and H. H. Patel, *Two-loop effective potential for generalized gauge fixing*, *Phys. Rev. D* **98** (2018) 076008, [[1808.07615](#)].
- [76] M. Laine, *The Two loop effective potential of the 3-d $SU(2)$ Higgs model in a general covariant gauge*, *Phys. Lett. B* **335** (1994) 173–178, [[hep-ph/9406268](#)].
- [77] A. J. Andreassen, *Gauge Dependence of the Quantum Field Theory Effective Potential*, Master’s thesis, Norwegian U. Sci. Tech., 2013.
- [78] A. Andreassen, W. Frost and M. D. Schwartz, *Consistent Use of the Standard Model Effective Potential*, *Phys. Rev. Lett.* **113** (2014) 241801, [[1408.0292](#)].
- [79] A. Andreassen, W. Frost and M. D. Schwartz, *Consistent Use of Effective Potentials*, *Phys. Rev. D* **91** (2015) 016009, [[1408.0287](#)].
- [80] L. Dolan and R. Jackiw, *Symmetry behavior at finite temperature*, *Phys. Rev. D* **9** (Jun, 1974) 3320–3341.
- [81] N. Nielsen, *On the Gauge Dependence of Spontaneous Symmetry Breaking in Gauge Theories*, *Nucl. Phys. B* **101** (1975) 173–188.
- [82] J. Fleischer and F. Jegerlehner, *Radiative Corrections to Higgs Decays in the Extended Weinberg-Salam Model*, *Phys. Rev. D* **23** (1981) 2001–2026.
- [83] J. Braathen, M. D. Goodsell, S. Paßehr and E. Pinsard, *Expectation management*, *Eur. Phys. J. C* **81** (2021) 498, [[2103.06773](#)].
- [84] A. Ekstedt and J. Löfgren, *On the relationship between gauge dependence and IR divergences in the \hbar -expansion of the effective potential*, *JHEP* **01** (2019) 226, [[1810.01416](#)].
- [85] G. W. Anderson and L. J. Hall, *The Electroweak phase transition and baryogenesis*, *Phys. Rev. D* **45** (1992) 2685–2698.
- [86] A. Megevand and A. D. Sanchez, *Supercooling and phase coexistence in cosmological phase transitions*, *Phys. Rev. D* **77** (2008) 063519, [[0712.1031](#)].
- [87] T. Alanne, T. Hugle, M. Platscher and K. Schmitz, *A fresh look at the gravitational-wave signal from cosmological phase transitions*, *JHEP* **03** (2020) 004, [[1909.11356](#)].
- [88] A. Ashoorioon and T. Konstandin, *Strong electroweak phase transitions without collider traces*, *JHEP* **07** (2009) 086, [[0904.0353](#)].
- [89] K.-P. Xie, *Lepton-mediated electroweak baryogenesis, gravitational waves and the 4π final state at the collider*, *JHEP* **02** (2021) 090, [[2011.04821](#)].

- [90] R. R. Parwani, *Resummation in a hot scalar field theory*, *Phys. Rev. D* **45** (1992) 4695, [[hep-ph/9204216](#)].
- [91] P. B. Arnold and O. Espinosa, *The Effective potential and first order phase transitions: Beyond leading-order*, *Phys. Rev. D* **47** (1993) 3546, [[hep-ph/9212235](#)].
- [92] P. M. Schicho, T. V. I. Tenkanen and J. Österman, *Robust approach to thermal resummation: Standard Model meets a singlet*, *JHEP* **06** (2021) 130, [[2102.11145](#)].
- [93] L. Niemi, P. Schicho and T. V. I. Tenkanen, *Singlet-assisted electroweak phase transition at two loops*, *Phys. Rev. D* **103** (2021) 115035, [[2103.07467](#)].
- [94] P. Athron, J.-h. Park, D. Stöckinger and A. Voigt, *FlexibleSUSY—A spectrum generator for supersymmetric models*, *Comput. Phys. Commun.* **190** (2015) 139–172, [[1406.2319](#)].
- [95] P. Athron, M. Bach, D. Harries, T. Kwasnitza, J.-h. Park, D. Stöckinger et al., *FlexibleSUSY 2.0: Extensions to investigate the phenomenology of SUSY and non-SUSY models*, *Comput. Phys. Commun.* **230** (2018) 145–217, [[1710.03760](#)].
- [96] F. Staub, *From Superpotential to Model Files for FeynArts and CalcHep/CompHep*, *Comput. Phys. Commun.* **181** (2010) 1077–1086, [[0909.2863](#)].
- [97] F. Staub, *Automatic Calculation of supersymmetric Renormalization Group Equations and Self Energies*, *Comput. Phys. Commun.* **182** (2011) 808–833, [[1002.0840](#)].
- [98] F. Staub, *SARAH 3.2: Dirac Gauginos, UFO output, and more*, *Computer Physics Communications* **184** (2013) pp. 1792–1809, [[1207.0906](#)].
- [99] F. Staub, *SARAH 4 : A tool for (not only SUSY) model builders*, *Comput. Phys. Commun.* **185** (2014) 1773–1790, [[1309.7223](#)].
- [100] B. C. Allanach, *SOFTSUSY: a program for calculating supersymmetric spectra*, *Comput. Phys. Commun.* **143** (2002) 305–331, [[hep-ph/0104145](#)].
- [101] B. Allanach, P. Athron, L. C. Tunstall, A. Voigt and A. Williams, *Next-to-Minimal SOFTSUSY*, *Comput. Phys. Commun.* **185** (2014) 2322–2339, [[1311.7659](#)].
- [102] C. P. D. Harman and S. J. Huber, *Does zero temperature decide on the nature of the electroweak phase transition?*, *JHEP* **06** (2016) 005, [[1512.05611](#)].
- [103] E. Senaha, *Radiative Corrections to Triple Higgs Coupling and Electroweak Phase Transition: Beyond One-loop Analysis*, *Phys. Rev. D* **100** (2019) 055034, [[1811.00336](#)].

- [104] T. Biekötter, S. Heinemeyer, J. M. No, M. O. Olea and G. Weiglein, *Fate of electroweak symmetry in the early Universe: Non-restoration and trapped vacua in the N2HDM*, *JCAP* **06** (2021) 018, [[2103.12707](#)].
- [105] A. Fowlie, *A fast C++ implementation of thermal functions*, *Comput. Phys. Commun.* **228** (2018) 264–272, [[1802.02720](#)].
- [106] C. L. Wainwright, *CosmoTransitions: Computing Cosmological Phase Transition Temperatures and Bubble Profiles with Multiple Fields*, *Comput. Phys. Commun.* **183** (2012) 2006–2013, [[1109.4189](#)].